



Longitudinal stress induced by basal slippery patch

Joshua Harlan Rines (1,2), jrines@stanford.edu

Ching-Yao Lai (1,2)

Yongji Wang (1,2,3)

1. Department of Geophysics, Stanford University
2. Department of Geosciences, Princeton University
3. Department of Mathematics, New York University

This manuscript has been submitted to the Journal of Glaciology for review

Peer review status:

This is a non-peer-reviewed preprint submitted to EarthArXiv.

Longitudinal stress induced by basal slippery patch

Joshua H. RINES,^{1,2} Ching-Yao LAI,^{1,2} Yongji WANG,^{1,2,3}

¹*Department of Geophysics, Stanford University, Stanford, CA, USA*

²*Department of Geosciences, Princeton University, Princeton, NJ, USA*

³*Department of Mathematics, New York University, New York, NY, USA*

Correspondence: Joshua H. Rines <jrines@stanford.edu>

ABSTRACT. Supraglacial lake drainages create spatially finite regions of reduced basal friction, slippery patches, at the ice-bed interface that perturb local stresses in the overlying ice, potentially sufficiently to trigger cascading hydrofracture-driven lake drainage events. We derive analytical solutions for the perturbed stress response to such slippery patches using the shallow shelf approximation and validate these solutions against 2d full-Stokes numerical simulations for Newtonian $n = 1$ and Glen $n = 3$ rheologies, spanning a range of flow parameters. The stress perturbation magnitude scales as $\rho g \alpha \ell / 4$, linear in surface slope α and patch length ℓ , and decays exponentially into the ice away from the patch over a decay lengthscale $(2Bh/C)^{n/(n+1)}$, dependent on ice thickness h , rheological parameters n, B , and basal sliding coefficient outside the patch, C . The stress decay lengthscale increases with larger ice thickness and smaller basal traction. Combining stress magnitude and decay lengthscale, we define an absolute coupling length as the distance over which the perturbed stress remains above a given threshold, which is largest in the Greenland ablation zone. We discuss implications of these results for the magnitude and spatial reach of stress communication among lake drainage events, especially under a warming climate.

25 **INTRODUCTION**

26 Interfaces between varying boundary conditions are critical to ice sheet dynamics. For example, the
27 organization of ice flow into ice streams, which serve as fast flowing conduits through which Antarctic
28 ice is rapidly transported seaward (e.g., Bindshadler and Vornberger, 1998; Hulbe and Fahnestock, 2007;
29 Rignot and others, 2011), is dependent on the dynamics associated with a transition in basal boundary
30 condition (Jacobson and Raymond, 1998; Suckale and others, 2014; Mantelli and others, 2019). The flux
31 of ice through the grounding line (e.g., off the edge of the continent to form floating ice shelves in the
32 ocean) is critically dependent on the dynamics at the basal boundary transition of the grounding line
33 (Weertman, 1974; Chugunov and Wilchinsky, 1996; Schoof, 2007a). Another such glacial interface is a
34 seasonally occurring feature of the Greenland Ice Sheet (GrIS): rapid spatially finite injections of surface
35 meltwater to the ice-bed interface from the drainage of supraglacial lakes through the ice column (e.g., Das
36 and others, 2008; Tsai and Rice, 2010; Stevens and others, 2015).

37 During the summer months (June-September) the GrIS ice-bed interface becomes partially lubricated
38 by surface meltwater which penetrates the ice column via surface-to-bed pathways such as moulins and
39 hydrofracture-driven lake drainages (HLD) (e.g., Alley and others, 2005; Das and others, 2008). These
40 spatially-finite injections of meltwater reduce the friction between the ice and bed below, leading to a tran-
41 sient acceleration of the overlying ice (Joughin and others, 2013; Stevens and others, 2016). In many cases,
42 the resulting induced stresses are sufficient to trigger further HLD events, delivering further lubricating
43 water to the bed (Das and others, 2008; Stevens and others, 2015; Christoffersen and others, 2018; Poinar
44 and Andrews, 2021). These rapid HLD events can deliver large volumes of water ($\sim 5 \times 10^7 \text{ m}^3$) to the
45 bed (Fitzpatrick and others, 2014), which form spatially-finite blisters of diameter on the order of several
46 ice thicknesses beneath the ice, reducing the effective pressure (ice overburden minus basal water pressure)
47 over that area (e.g., Lai and others, 2021; Stevens and others, 2024).

48 In some cases, multiple neighboring lakes are observed to drain in rapid succession leading to the
49 hypothesis of a domino effect of HLD events, where one lake drainage may trigger another and so on,
50 which could have the capacity to then transiently overwhelm the evacuation capacity of the subglacial
51 hydrological system, leading to increased ice motion (e.g., Christoffersen and others, 2018). Prescience
52 of these dynamics is especially relevant as the presence of lakes is projected to expand inland over the
53 coming decades in response to the warming climate (Leeson and others, 2015; Ignéczi and others, 2016;

54 MacFerrin and others, 2019). These inland regions are characterized by a subglacial hydrological system
55 which may be more readily overwhelmed by meltwater injections due to thicker more gently sloping ice,
56 potentially leading to a lower effective basal friction in response to rapid basal meltwater injection (e.g.,
57 HLD) (Chandler and others, 2013; Meierbachtol and others, 2013; Dow and others, 2014; Doyle and others,
58 2014). Constraining the structure of the influence one lake drainage has on other lakes in the area via distal
59 stress communication, and how this communication varies across the GrIS, remains a critical yet incomplete
60 challenge. In this study, we aim to investigate the following question: what are the fundamental controls
61 on the magnitude and spatial extent of stress and velocity response to spatially finite basal traction loss?

62 Our case sits within a broader class of ice flow problems subjected to spatially varying basal boundary
63 conditions. For grounded ice sheets this type of transition often occurs at the onset (margins) of narrow
64 rapidly moving regions, known as ice streams, which are fed laterally by slower moving ice ridges that are
65 basally frozen. Jacobson and Raymond (1998) demonstrated the sensitivity of ice stream margin locations
66 to thermo-viscous feedbacks. Haseloff and others (2015) derive a boundary layer description of this lateral
67 transition from slow shear-type to fast plug-type flow, accounting for the role of lateral advection on margin
68 migration. Barcilon and MacAyeal (1993) describe the structure of flow across an along-flow basal condition
69 transition from no-slip to free-slip, work which was extended by Mantelli and others (2019) and Schoof and
70 Mantelli (2021) to include the thermomechanical behavior in the associated boundary layers. The present
71 paper differs in that we discuss a spatially finite region of rapid flow with an upstream transition from
72 slow to fast flow and a downstream transition back to slow flow. We are also interested in systems for
73 which the slippery region is not induced or controlled thermomechanically, rather simply by the presence
74 of meltwater which can supply sufficient upward pressure on the overlying ice to drastically reduce basal
75 friction, such as is the case following a rapid lake drainage (e.g., Lai and others, 2021).

76 Previous attention has been paid to the problem of ice flow over spatially finite basal heterogeneities.
77 Several studies demonstrate steady-state longitudinal transmission of basal heterogeneities (e.g., topog-
78 raphy) to be on the order of several ice thicknesses (e.g., Kamb and Echelmeyer, 1986; Gudmundsson,
79 2003; Raymond and Gudmundsson, 2005; Sergienko, 2013; Crozier and others, 2018). In particular, Gud-
80 mundsson (2003) investigates surface responses to small amplitude basal slipperiness perturbations, finding
81 regions of extension and compression up and downstream from the basal heterogeneity, respectively, quali-
82 tatively consistent with our findings. Gudmundsson (2008) uses the shallow shelf approximation (SSA) to
83 derive analytical transfer functions for small amplitude sinusoidal basal slipperiness perturbations in the

84 Newtonian limit, which imply exponentially decaying spatial responses, consistent with our work. Here, we
 85 aim to add to this conversation by posing a boundary value problem for a spatially finite slippery patch,
 86 deriving the lengthscale of the boundary layer adjacent to a slippery patch for linear and non-linear rheol-
 87 ogy. Using a simple analytical model and scaling arguments, we reveal the dominant relationships between
 88 geometrical parameters (ice thickness, slope, patch length) and the resulting stress and velocity perturba-
 89 tions. In this paper, we do not evolve the system forward in time, as the slippery patch-induced stress
 90 perturbations are directly relevant for triggering surface fracture and potential subsequent lake drainage
 91 cascades. However, long-term impacts of the slippery patch’s annual appearance on ice-sheet dynamics
 92 remains an interesting direction for future work.

93 We begin by presenting our model, which is a simplified representation of the stress coupling from lake
 94 drainage-induced basal sliding. We present an analytical model based on the SSA (MacAyeal, 1989), as
 95 well as 2d numerical simulations. We then discuss the implications of this work in the context of Greenland
 96 Ice Sheet lake drainages under the warming climate before concluding the paper.

97 **MODEL**

98 We consider an idealized 2d (along-flow) ice sheet, which is of infinite length, constant thickness and surface
 99 slope, and flowing from left to right. In the interior of the domain exists a patch of finite length across which
 100 the basal boundary condition is shear-free, that is, a “slippery patch” (figure 1). As a further simplification,
 101 we consider a depth-integrated version of this model, which admits elementary analytical solutions. We
 102 present each of these models, in turn, below. We present this first, before moving to a demonstration of
 103 the 2d system, which is solved numerically.

104 **Numerical model (2d)**

We consider a 2-dimensional flowline numerical model. We use the open-source finite element full-Stokes
 solver Elmer/Ice (Gagliardini and others, 2013), with which we conducted a suite of numerical experiments.
 In particular, we used Elmer/Ice to solve the incompressible Stokes system:

$$\nabla \cdot \boldsymbol{\sigma} + \rho_i \mathbf{g} = \mathbf{0}, \quad \nabla \cdot \mathbf{u} = 0, \quad (1)$$

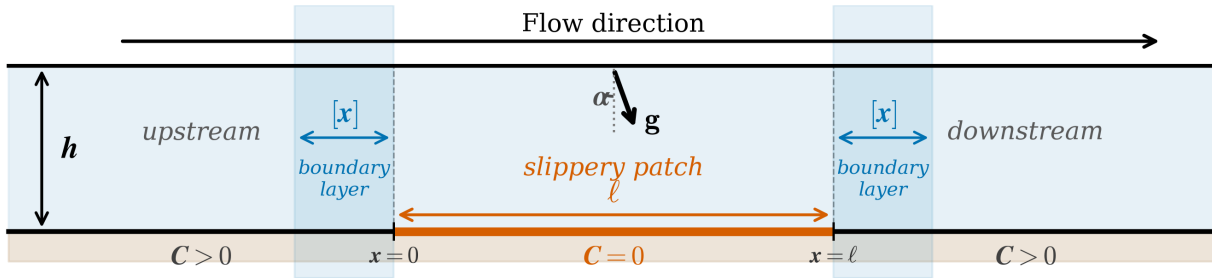


Fig. 1. Schematic of the 2d flowline model. An ice slab of uniform thickness h flows over a bed with a spatially finite slippery patch of length ℓ (orange) where basal friction coefficient $C, C_b = 0$. Outside the patch, the bed has finite friction $C, C_b > 0$ set by the sliding ratio γ . Boundary layers on the up- and downstream edges of the patch, where the flow transitions from free slip to basal friction conditions. The surface slope α defines the gravitational driving stress $\tau_d = \rho g h \alpha$.

105 in a domain of length L_x , subjected to periodic boundary conditions on both the horizontal (x) and vertical
 106 (z) components of the velocity field, $u(x, z)$ and $w(x, z)$, respectively. The simulation mesh is structured
 107 with spatially varying horizontal resolution across five zones: fine resolution (10 m) across the center 50
 108 km of the domain, intermediate resolution (100 m) in 50 km zones on both sides adjacent to the central
 109 region, and coarse resolution (500 m) in the far-field beyond. The mesh is extruded vertically to the ice
 110 thickness h with 40 vertical levels.

We ran a suite of experiments designed to investigate the relationship between the geometrical parameters of the flow and the resulting stress response. We later compare these empirical relationships to those that arise from the analytical model. To this end, we ran simulations over a range of parameter values for the ice thickness h , surface slope α , patch length ℓ , and basal sliding states γ, C_b (table 1). Basal sliding is characterized by a Weertman-type (e.g., Weertman, 1957) sliding law of the form

$$\tau_b = C_b |u_b|^{1/n-1} u_b, \quad (2)$$

where the subscript b indicates quantities basal interface and we follow a common simplification of the Weertman sliding law, taking the exponent to be $1/n$ (e.g., Weertman, 1974; Schoof, 2007b; Tsai and others, 2015; Sergienko, 2022), where n is the flow law exponent in Glen's flow law (Glen, 1955). Here, we define γ as the ratio between the scales of sliding and deformation contributions to velocity, that facilitates

Table 1. Range of parameter values used in the numerical experiments.

Parameter	Symbol	Value(s)	Units
Ice thickness	h	[0.3, 1.0, 2.0, 3.0]	km
Surface (bed) slope	α	[0.1, 0.5, 1.0]	°
Patch length	ℓ	[2.5, 5.0, 10.0, 25.0]	km
Flow law exponent	n	1 or 3	–
Flow law parameter	B^{-n}	$\begin{cases} 5.0 \times 10^{-15} & (n = 1) \\ 2.4 \times 10^{-24} & (n = 3) \end{cases}$	$\text{Pa}^{-n} \text{s}^{-1}$
Sliding ratio	γ	[0.1, 0.5]	–
Basal sliding coefficient	C_b	$B(\gamma/h)^{1/n}$	$\text{Pa s}^{1/n} \text{m}^{-1/n}$

later comparison to the analytical model strictly valid when $\gamma \ll 1$,

$$\gamma \equiv \frac{[u_{\text{deform}}]}{[u_{\text{slide}}]} = \frac{B^{-n} \tau_b^n h}{(\tau_b/C_b)^n} = \frac{h C_b^n}{B^n}, \quad (3)$$

111 where the brackets $[\]$ indicate characteristic scale of the variable inside the brackets. All experiments were
 112 conducted with an ice sheet of constant thickness and surface slope (simply by tilting the gravity vector
 113 acting upon the flow according to α , see e.g., figure 1) and were subjected to periodic boundary conditions
 114 at the inflow (left) and outflow (right) of the ice body. We repeated this experiment for two ice rheologies:
 115 Newtonian ($n = 1$) and Glen ($n = 3$). The flow, in both cases, results in a strong perturbation in the
 116 velocity and stress fields at the center of the domain where the slippery patch resides, but returns to the
 117 background flow state, consistent with sliding-accommodated SIA, toward the edges of the domain (figure
 118 2).

119 Analytical model (1d)

To derive the 1d model, we begin this section by considering the depth-integrated shallow stream approx-
 imation (SSA) (MacAyeal, 1989)

$$\partial_x(2h\tau_{xx}) - \tau_b - \rho g h \partial_x s = 0, \quad (4)$$

where g is gravity, h , ρ , s are ice thickness, density, and surface, respectively, τ_{xx} is longitudinal deviatoric
 stress, and τ_b is the basal traction. This approximation of Stokes requires a dominant contribution of sliding

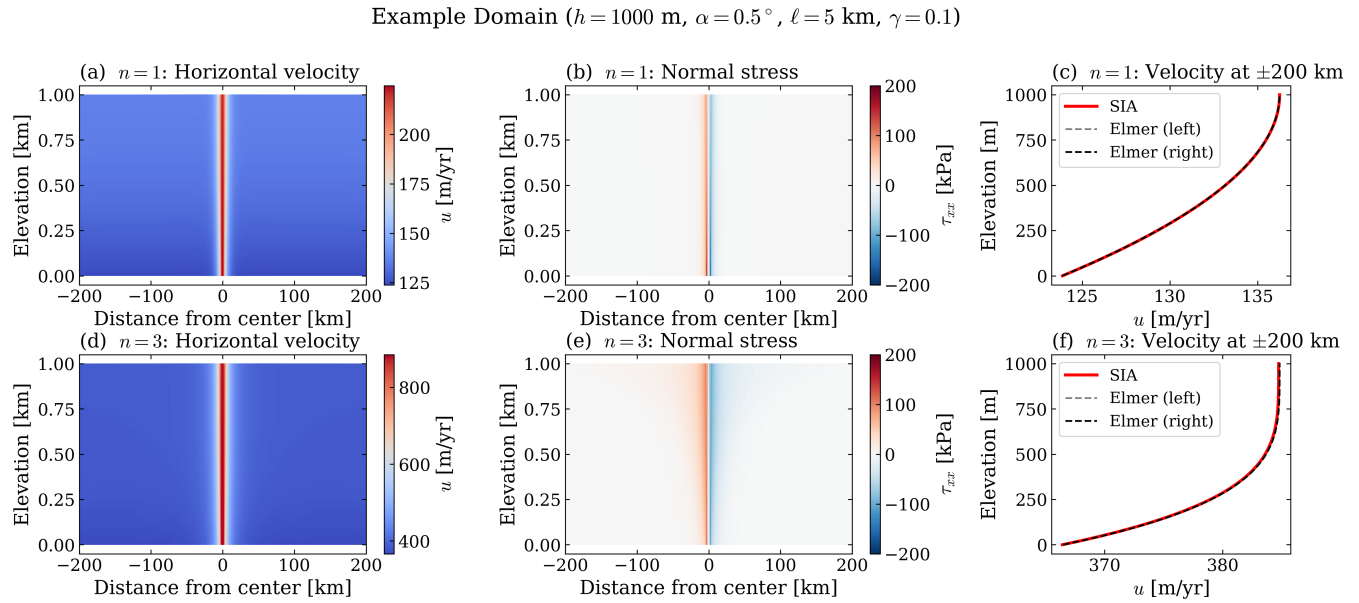


Fig. 2. Example simulation domain for $h = 1000$ m, $\alpha = 0.5^\circ$, $\ell = 5$ km, $\gamma = 0.1$. (a, d) Horizontal velocity field $u(x, z)$ response to the slippery patch for Newtonian $n = 1$ and Glen $n = 3$ rheologies, respectively. (b, e) Deviatoric normal stress $\tau_{xx}(x, z)$ response to the slippery patch for Newtonian and Glen rheologies, respectively. (c, f) Vertical profiles of horizontal velocity at the (periodic) inflow/outflow (dashed) boundaries compared to analytical basal sliding-accommodated SIA solution (red).

to the overall velocity, namely $\gamma \ll 1$ (3). As mentioned above (and in Appendix A), this depth-integrated model uses the following parameterization for the basal shear term:

$$\tau_b = C|u|^{1/n-1}u, \quad (5)$$

where C, u are depth-integrated quantities with $C = C_b(u_b/u)^{1/n}$ (51) relating the depth integrated quantity C in our 1d model with the basal quantities C_b, u_b from the Elmer/Ice simulations. The flow law exponent n comes from Glen's flow law (Glen, 1955), which relates the strain rate to the applied stress as

$$\tau_{xx} = B|\dot{\epsilon}_{xx}|^{1/n-1}\dot{\epsilon}_{xx}, \quad (6)$$

with B the ice hardness parameter and $\dot{\epsilon}_{xx} = \partial_x u$ the deviatoric strain rate, where u is horizontal velocity. We take the simplifying case of constant ice thickness and surface slope, $s_x = -\alpha$. With these relationships, we rewrite the SSA equation in terms of velocity as

$$2Bh(|u_x|^{1/n-1}u_x)_x - C|u|^{1/n-1}u + \rho gh\alpha = 0, \quad (7)$$

where derivatives are here and henceforth denoted with subscripts. The basal traction condition is piecewise constant across the domain:

$$C(x) = \begin{cases} 0, & x \in [0, \ell], \\ C > 0, & x \in (-\infty, 0] \cup [\ell, \infty). \end{cases} \quad (8)$$

We are predominantly interested in the spatial structure of the perturbed stress which arises from the presence of a spatially-finite patch of free-slip. Our model considers the stress profile across the patch as setting the boundary condition for the surrounding boundary layers upstream and downstream from the patch. Inside the patch $C = 0$ and the SSA reduces to

$$(2h\tau_{xx})_x = -\tau_d, \quad x \in [0, \ell] \quad (9)$$

where the $\tau_d = \rho gh\alpha$ is the driving stress. Independent of n , this yields a linear membrane stress profile

across the patch (see also Figure 4b,f, middle panel):

$$\tau_{xx}(x) = \tau_{xx}(0) - \frac{\tau_d}{2h}x. \quad (10)$$

The antisymmetry of the membrane stress about the patch center, $\tau_{xx}(\ell/2) = 0$, gives the boundary condition at the upstream patch edge:

$$\tau_{xx}(0) = -\tau_{xx}(\ell) = \frac{\tau_d \ell}{4h} = \frac{\rho g \alpha \ell}{4} \quad (11)$$

such that equation (10) can be rewritten as

$$\tau_{xx} = \frac{\rho g \alpha \ell}{4} \left(1 - 2\frac{x}{\ell}\right) \quad (12)$$

yielding a characteristic scale for the stress perturbation $[\tau_{xx}]$:

$$[\tau_{xx}] \equiv \frac{\rho g \alpha \ell}{4} \quad (13)$$

Outside the patch where our basal traction is given by $C(x) = C$, the governing equation is

$$(2h\tau_{xx})_x - C|u|^{1/n-1}u = -\tau_d, \quad x \in (-\infty, 0] \cup [\ell, \infty) \quad (14)$$

subjected to the boundary condition above (11). Using the constitutive relation $\tau_{xx} = B|u_x|^{1/n-1}u_x$, the relevant length and velocity scales of this region can be found from the balance between deviatoric stress gradient and basal drag terms in (7):

$$\frac{2Bh[u]^{1/n}}{[x]^{1/n} \cdot [x]} = C[u]^{1/n}, \quad (15)$$

from which $[u]^{1/n}$ cancels, giving the characteristic lengthscale of this region:

$$[x] = \left(\frac{2Bh}{C}\right)^{\frac{n}{n+1}}. \quad (16)$$

This region is host to a boundary layer (BL) at the edge (upstream and downstream) of the patch, where the flow transitions from the far field, which is characterized by a balance between basal drag and driving stress to the patch interior, which is characterized by a balance between longitudinal stresses and driving

stress. Thus, across this boundary layer, there is a balance between longitudinal stresses and basal drag. The velocity scale is then determined by the membrane stress boundary condition at $x = 0$ (11):

$$2Bh \frac{[u]^{1/n}}{[x]^{1/n}} = \frac{\tau_d \ell}{2}, \quad (17)$$

which gives

$$[u] = [x] \left(\frac{\tau_d \ell}{4Bh} \right)^n = [x] \left(\frac{\rho g \alpha \ell}{4B} \right)^n. \quad (18)$$

Nondimensionalizing with

$$u = [u] \tilde{u} \quad (19)$$

$$x = [x] \tilde{x} \quad (20)$$

$$\tau_{xx} = [\tau_{xx}] \tilde{\tau}_{xx} \quad (21)$$

with $[u]$, $[x]$, and $[\tau_{xx}]$ defined in equations 18, 16, and 13 respectively, gives the dimensionless governing equation outside the patch:

$$(|\tilde{u}_{\tilde{x}}|^{1/n-1} \tilde{u}_{\tilde{x}})_{\tilde{x}} - |\tilde{u}|^{1/n-1} \tilde{u} = -2\delta, \quad (22)$$

where

$$\delta \equiv \frac{[x]}{\ell} = \frac{(2Bh/C)^{n/(n+1)}}{\ell} \quad (23)$$

is the ratio of the boundary layer extent to the patch length. Here, we decompose the velocity into a sum of two components, namely the background far-field velocity u_∞ and the perturbed boundary layer velocity u' . We do this in order to facilitate later comparison between this analytical solution and the depth-averaged numerical simulations with the background velocity subtracted away. In particular, we take

$$u(x) = u_\infty + u'(x), \quad (24)$$

and introduce a dimensionless variable relating these two components' scales

$$\varepsilon \equiv \frac{u_\infty}{[u]}, \quad (25)$$

such that we have

$$\tilde{u}(\tilde{x}) = \varepsilon + \tilde{u}'(\tilde{x}). \quad (26)$$

Substitution into the dimensionless governing equation, noting that $\tilde{u}_{\tilde{x}} = \tilde{u}'_{\tilde{x}}$, gives

$$(|\tilde{u}'_{\tilde{x}}|^{1/n-1} \tilde{u}'_{\tilde{x}})_{\tilde{x}} - |\varepsilon + \tilde{u}'|^{1/n-1} (\varepsilon + \tilde{u}') = -2\delta. \quad (27)$$

We note that the dimensionless background balance, obtained by evaluating the governing equation far from the patch where $\tilde{u}' \rightarrow 0$, requires

$$|\varepsilon|^{1/n-1} \varepsilon = 2\delta, \quad (28)$$

which allows us to rewrite the governing equation as:

$$(|\tilde{u}'_{\tilde{x}}|^{1/n-1} \tilde{u}'_{\tilde{x}})_{\tilde{x}} = |\varepsilon + \tilde{u}'|^{1/n-1} (\varepsilon + \tilde{u}') - |\varepsilon|^{1/n-1} \varepsilon. \quad (29)$$

For $n = 1$, the right-hand side simplifies exactly: $(\varepsilon + \tilde{u}') - \varepsilon = \tilde{u}'$, independent of ε . For $n > 1$, since $\varepsilon = (2\delta)^n \ll 1$ when $\delta \ll 1$ (28), the right-hand side of (29) reduces to $|\tilde{u}'|^{1/n-1} \tilde{u}'$, giving the leading-order boundary layer equation (dropping tildes henceforth):

$$(|u'_x|^{1/n-1} u'_x)_x = |u'|^{1/n-1} u', \quad (30)$$

which is subjected to the following boundary conditions:

$$u' = 0 \quad (x \rightarrow -\infty) \quad (31)$$

$$|u'_x|^{1/n-1} u'_x = 1 \quad (x = 0), \quad (32)$$

120 where (32) is the dimensionless version of (11).

Taking typical scales of $h \sim 10^3$ m, $\ell \sim 10^4$ m, $B \sim 7.5 \times 10^7$ Pa s^{1/3}, $C \sim 5 \times 10^6$ Pa s^{1/3} m^{-1/3} gives $[x] \sim 2.3 \times 10^3$ m (16). In order to strictly use SSA to describe this system, we must have $h \ll [x] \ll \ell$. With the scales estimated from above, we have $h \sim 1 \times 10^3$ m, $[x] \sim 2.3 \times 10^3$ m, and $\ell \sim 10^4$ m, meaning $\delta \sim 0.23$. While the parameter combinations may not place us in deeply in the asymptotic regime of $\delta \ll 1$, the resulting reduced-order model is reasonable, illustrative, and interpretable, but not asymptotically strict. Thus, the remainder of this derivation shall be concerned with evaluating analytically the system

under these assumptions, but note that the boundary layer scaling (16) sufficiently captures relationships outside this parameter regime (see, e.g., figure 4c,d,g,h). For convenience, we define

$$y \equiv |u'_x|^{1/n-1} u'_x \quad (33)$$

$$\Rightarrow u'_x = |y|^{n-1} y, \quad (34)$$

which allows us to write our leading-order governing equation as

$$u'_x \frac{d}{du'} (|u'_x|^{1/n-1} u'_x) = |y|^{n-1} y \frac{dy}{du'} = |u'|^{1/n-1} u' \quad (35)$$

$$\Rightarrow \frac{1}{n+1} \frac{d}{du'} (|y|^{n+1}) = |u'|^{1/n-1} u'. \quad (36)$$

Integration of this equation (and applying the boundary condition from (31)) yields

$$|y|^{n+1} = n |u'|^{1/n+1} \quad (37)$$

$$\Rightarrow u'_x = |y|^{n-1} y = n^{\frac{n}{n+1}} |u'|^{1-1/n} u'^{1/n}, \quad (38)$$

where we can drop the absolute values given the solution (subjected to the boundary conditions) will be positive everywhere, and we write, for simplicity:

$$u'_x = n^{\frac{n}{n+1}} u', \quad (39)$$

Integration of the ODE gives

$$u'(x) = u'_0 \exp(n^{\frac{n}{n+1}} x), \quad (40)$$

where $u'_0 = \left(\frac{1}{n}\right)^{\frac{n}{n+1}}$ is determined by the boundary condition at $x = 0$. To illustrate, we start with

$$|y|^{n+1} = n |u'|^{1/n} \quad (41)$$

and recognize that the boundary condition at $x = 0$, $|u'_x|^{1/n-1} u'_x = 1$, is just $y(0) = 1$ in terms of y . Then,

letting $u'_0 \equiv u'(0)$:

$$|y(0)|^{n+1} = 1^{n+1} = n|u'_0|^{\frac{n+1}{n}} \quad (42)$$

$$\Rightarrow u'_0 = \left(\frac{1}{n}\right)^{\frac{n}{n+1}} \quad (43)$$

$$\Rightarrow u'(x) = \left(\frac{1}{n}\right)^{\frac{n}{n+1}} \exp\left(n^{\frac{n}{n+1}} x\right) \quad (44)$$

This gives the velocity structure in the boundary layer (as discussed further in Appendix B). For the deviatoric stress, we use the constitutive relation in dimensionless form (tildes dropped):

$$\tau_{xx} = |u'_x|^{1/n-1} u'_x = y(x). \quad (45)$$

Substituting the velocity solution gives the dimensionless stress decay profile:

$$\tau_{xx}(x) = n^{\frac{1}{(n+1)}} (u'(x))^{\frac{1}{n}} = \exp\left(n^{-\frac{1}{(n+1)}} x\right), \quad (46)$$

121 where we drop the absolute values signs because $u' > 0$ and $u'_x > 0$ in the upstream boundary layer.
 122 Downstream from the trailing edge of the patch ($x = \ell$), the stress profile is solved for in the same way,
 123 with the stress decaying at the same rate into $x > \ell$.

124 Summary

In summary, the relevant spatial scale for the stress perturbation differs across the domain. Namely, $[x]$ (16) dictates the stress decay lengthscale upstream and downstream from the patch (equation (46)), and ℓ characterizes the linear stress variation lengthscale across the patch interior (equation (12)). Returning to dimensional variables τ_{xx} and x , we write the summary for the deviatoric stress profile across the full domain:

$$\frac{\tau_{xx}(x)}{\rho g \alpha \ell / 4} = \begin{cases} \exp\left(n^{-\frac{1}{n+1}} \frac{x}{[x]}\right), & x \leq 0 \\ 1 - 2\frac{x}{\ell}, & 0 \leq x \leq \ell \\ -\exp\left(-n^{-\frac{1}{n+1}} \frac{(x-\ell)}{[x]}\right), & x \geq \ell \end{cases} \quad (47)$$

125 Inside the boundary layer regions, the spatial coordinate x is measured from the nearest patch edge and
 126 scaled by $[x]$ (16), while inside the patch the coordinate is measured from the upstream edge and scaled
 127 by the patch length ℓ . This analytical solution is rendered as the solid black curve in figure 4b,f.

128 RESULTS AND DISCUSSION

129 We first present an analysis of the stress response at the ice surface, which we extracted from the numerical
 130 experiments, before moving to compare the 1d model to the depth-integrated simulation results. We then
 131 discuss implications of this work. In all comparisons between the numerical results and analytical scalings,
 132 the depth-averaged friction coefficient C in the decay lengthscale $[x]$ (16) is obtained from the basal
 133 coefficient C_b via the relationship $C = C_b(u_b/u)^{1/n}$ (51), where C_b is specified in the Elmer/Ice simulations
 134 by the sliding ratio γ ((3), table 1).

135 Surface Stress

136 For the numerical experiments, we used the flow parameters that were presented in table 1. The stress
 137 at the ice surface exhibits regions of tension and compression on the upstream and downstream sides
 138 of the slippery patch, respectively (figure 3a,b). This is expected, as the ice accelerates across the first
 139 half of the patch due to the basal traction loss, and decelerates across the second half of the patch as
 140 it begins to feel the basal shear stress effects on the other side of the patch. Though our 1d analytical
 141 model does not apply to the ice surface stresses, we observed from the simulations that the analytical
 142 scaling relationships between the ice geometry (e.g., h, α, ℓ) and the stress response hold. In particular,
 143 the magnitude of the surface stress scales linearly with $\rho g \alpha \ell / 4$ and the decay length scales with $[x]$ (16)
 144 for experiments with Newtonian and Glen rheologies, albeit each with different prefactors. To obtain these
 145 prefactors, for each simulation, we compute the ratio of the simulated quantity to the theoretical scale (e.g.,
 146 $\max |\tau_{xx}^{\text{surf}}| / (\rho g \alpha \ell / 4)$). The associated prefactor κ is then the median of those ratios across the ensemble of
 147 simulations, with gray bands spanning the 16th-84th percentiles. To quantify the decay lengthscales from
 148 the numerical experiments, we take the length upstream from the patch onset over which the perturbed
 149 stress is above $\max |\tau_{xx}| / e$ because the 1d model implies a decaying exponential function, so this is the
 150 natural measure of the associated decay lengthscale. The stress magnitude relates to the theoretical stress
 151 scale with prefactors of $\kappa_1 = 0.78$ and $\kappa_3 = 0.95$ for the Newtonian and Glen experiments, respectively,
 152 while the decay lengths relate to the theoretical decay lengthscale with prefactors of $\kappa_2 = 1.40$ and $\kappa_4 = 3.22$

153 for the Newtonian and Glen experiments, respectively. These prefactors are all $\mathcal{O}(1)$, indicating that, to
 154 the first order, the characteristic scales $[\tau_{xx}] \equiv \rho g \alpha \ell / 4$ and $[x] \equiv \left(\frac{2Bh}{C}\right)^{\frac{n}{n+1}}$ provide good estimates of
 155 surface stress magnitude and decay lengthscale, respectively.

156 We note that we restrict the analysis to simulations satisfying the minimum requirement of $h < [x] < \ell$,
 157 which ensures the boundary layer (decay) length scale is sufficiently broad such that we can reasonably
 158 use a depth-integrated model (i.e., SSA), but not broader than the slippery patch length ℓ . For the profile
 159 panels (Figure 3a,d), we further require that $\delta \equiv \frac{[x]}{\ell} < 0.3$ to display cases where boundary layers are
 160 well separated from the patch interior. The scaling panels (Figure 3b,c,e,f) include all simulations which
 161 satisfy the first filter ($h < [x] < \ell$). These two restrictions are likewise applied to our analysis of the
 162 depth-averaged stresses, below.

163 Depth-Averaged Stress

164 For the depth-averaged stresses we once again compare the scalings from the 1d model to results from
 165 the simulations, which we now have depth-averaged. The depth-averaged stress magnitude scales linearly
 166 with $\rho g \alpha \ell / 4$ and the decay length scales linearly with $[x]$ again for both rheologies with prefactors κ_5, κ_6
 167 and κ_7, κ_8 for Newtonian and Glen rheologies, respectively (figure 4c,d,g,h). The prefactor values for these
 168 depth-averaged results echo the patterns observed for the surface stresses, where the stress magnitudes are
 169 similar between rheologies ($\kappa_5 = 0.93, \kappa_7 = 0.94$ for Newtonian and Glen, respectively). The decay length
 170 prefactors show more discrepancy ($\kappa_6 = 1.04, \kappa_8 = 2.86$ for Newtonian and Glen, respectively).

171 The non-dimensionalized stress profiles also agree well with the 1d analytical model (figure 4b,f), con-
 172 firming the existence of up (down)stream boundary layers with exponential stress decay (recovery) and
 173 linear stress decline across the patch. The collapsed numerical profiles are tighter to the 1d analytical
 174 model for the Newtonian experiments than for the Glen experiments, consistent with and indeed expected
 175 from the model derivation (see, e.g., equations 25-30). In particular, for $n = 1$, the boundary layer equation
 176 is exact and the background velocity terms cancel identically, independent of δ . However for $n > 1$ this
 177 cancellation is approximate, strictly requiring $\epsilon = (2\delta)^n \ll 1$, leading to increasing error with increasing δ
 178 (see e.g., Figure C1). In figure 4(a, d) we only included simulations with $\delta < 0.3$. The simulations with
 179 Glen rheology are thus subject to two compounding effects: the approximation is inexact for $\delta > 0$ and δ is
 180 systematically larger due to the broader extent of the boundary layer for Glen rheologies, which degrades
 181 the agreement between the 1d model and the depth-averaged simulations with Glen rheology, though the

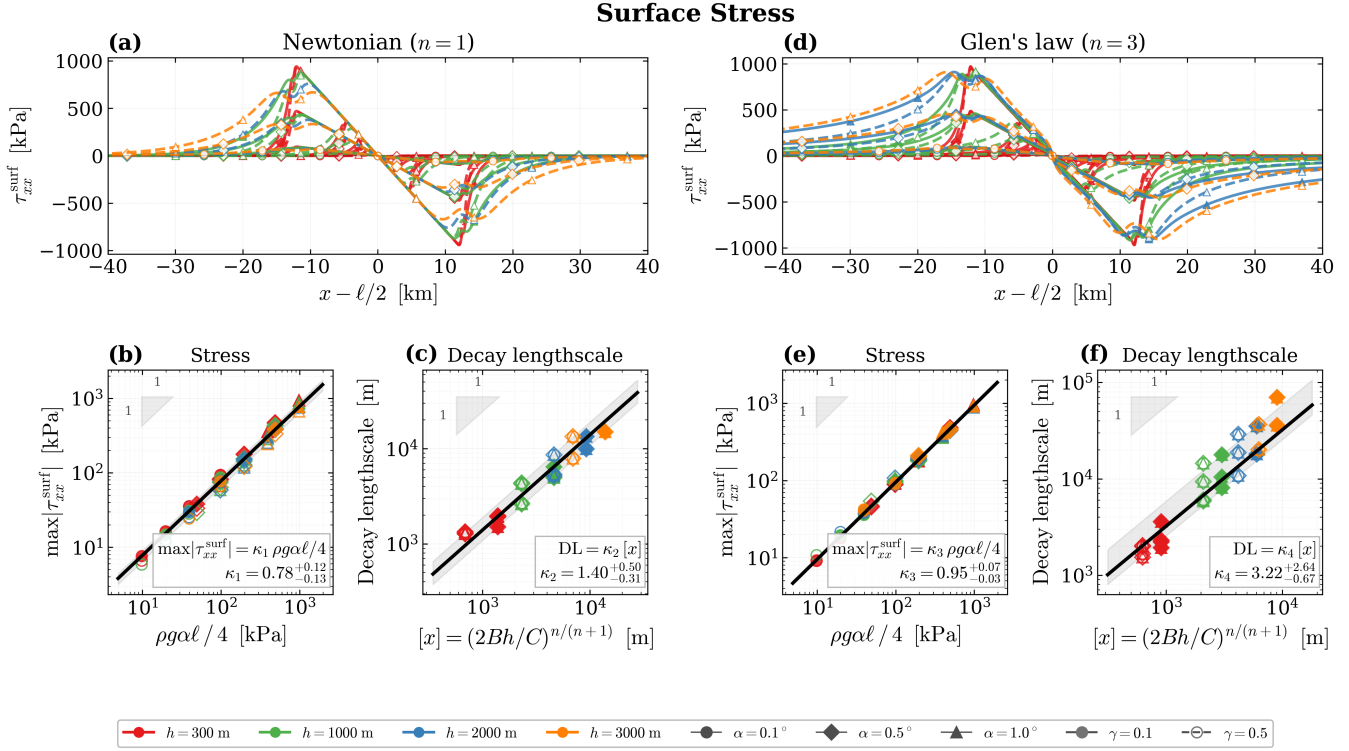


Fig. 3. Surface longitudinal stress τ_{xx}^{surf} from the 2d Elmer/Ice numerical simulation ensemble for Newtonian ($n = 1$, left) and Glen ($n = 3$, right) rheologies. (a, d) Dimensional surface stress profiles across the slippery patch, colored by ice thickness h with marker shape depicting surface slope α and linestyle depicting sliding ratio γ . Profiles with $\delta = [x]/\ell < 0.3$ are shown. (b, e) Maximum surface stress $\max|\tau_{xx}^{surf}|$ versus the analytical prediction $\rho g \alpha \ell / 4$ with proportionality constants κ_1 and κ_3 for Newtonian and Glen rheologies, respectively. (c, f) Decay lengthscale (DL; e-folding decay distance from the stress peak) versus the theoretical decay lengthscale $[x] = (2Bh/C)^{n/(n+1)}$ with κ_2 and κ_4 for Newtonian and Glen rheologies, respectively. Asymmetric error bounds (gray shade) denote the 16th-84th percentile of κ prefactor estimates. We have restricted the all plots, including the log-log plots to display simulation results satisfying $h < [x] < \ell$.

Table 2. Numerically determined prefactors κ for scaling relationships of maximum stress perturbation $\max(\tau_{xx})$ and decay lengthscale DL. DA and S denote depth-averaged and surface quantities, respectively. Values are medians across the simulation ensemble; superscripts and subscripts give the 16th–84th percentile bounds.

Case	$\max(\tau_{xx}) = \kappa [\rho g \alpha \ell / 4]$	DL = $\kappa \left[(2Bh/C)^{n/(n+1)} \right]$
$n = 1, S$	$\kappa_1 = 0.78_{-0.13}^{+0.12}$	$\kappa_2 = 1.40_{-0.31}^{+0.50}$
$n = 3, S$	$\kappa_3 = 0.95_{-0.03}^{+0.07}$	$\kappa_4 = 3.25_{-0.67}^{+2.64}$
$n = 1, DA$	$\kappa_5 = 0.93_{-0.07}^{+0.04}$	$\kappa_6 = 1.04_{-0.06}^{+0.56}$
$n = 3, DA$	$\kappa_7 = 0.93_{-0.06}^{+0.03}$	$\kappa_8 = 2.86_{-0.78}^{+0.64}$

182 overall agreement remains good across both rheologies. A summary of the prefactors for both surface and
 183 depth-averaged stresses is provided in table 2.

184 Implications

185 One benefit of a simple model such as ours is the ease with which we apply it to make qualitative im-
 186 plications. From the modeling work above, it is clear that the stress perturbation responding to a basal
 187 slippery patch is critically dependent on the ice thickness, surface slope, slippery patch length, and sur-
 188 rounding basal sliding conditions. The guiding question of ‘what is the structure of stress perturbations
 189 from slippery patches’ stems from the need to understand how the ice sheet might respond to continued
 190 arctic warming and meltwater forcings. In particular, our work was initially motivated by the lake drainage
 191 cascade hypothesis, whereby the stress perturbation resulting from the drainage of one lake might trigger
 192 the drainage of another (e.g., Christoffersen and others, 2018). The communication of stresses between
 193 lakes in response to their drainage is still yet to be fully understood. It remains unclear how and how far
 194 these stresses may be transmitted in response to HLD-induced meltwater injections (which we treat here as
 195 slippery patches). Modeling of membrane stress response to basal traction loss by Christoffersen and others
 196 (2018) suggests there may be a mechanism by which lakes located several tens of kilometers apart may
 197 transmit stresses and provide a sufficient triggering mechanism. Observations of HLD-induced stresses by
 198 Stevens and others (2024) suggest coupling lengthscale on the order of only several ice thicknesses. In this
 199 study, we have aimed to contribute to this ongoing conversation in the literature, using our simple model
 200 to reveal the structure of an idealized slippery patch-induced stress perturbation. As discussed above, we
 201 find that the magnitude of the stress perturbation is set by $\rho g \alpha \ell$, and decays into the upstream ice over a

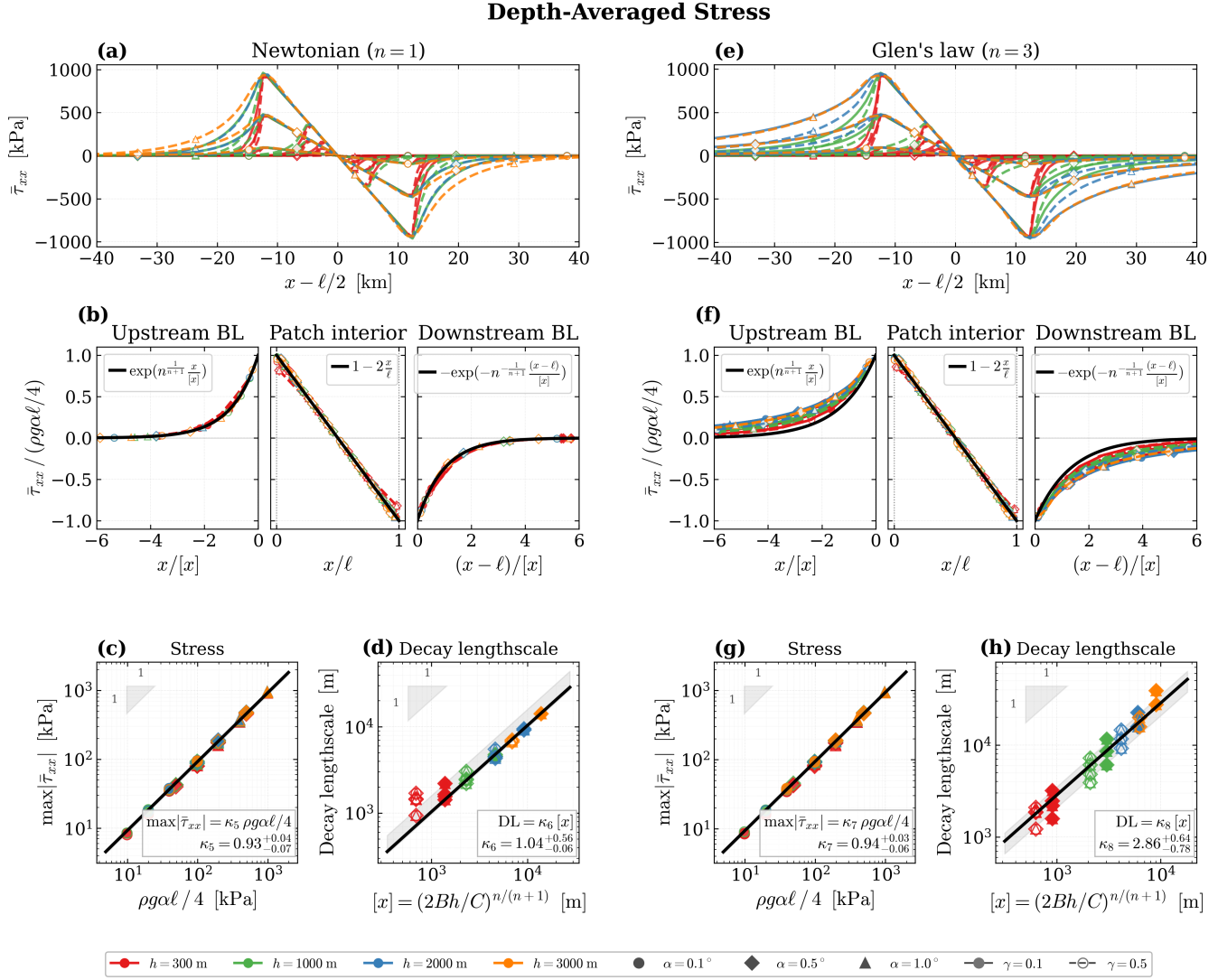


Fig. 4. Depth-averaged longitudinal stress $\bar{\tau}_{xx}$ from the 2d Elmer/Ice simulation ensemble for (left) Newtonian $n = 1$ and (right) Glen $n = 3$ rheologies. Top row (a, e): Dimensional profiles across the patch, colored by ice thickness h with marker shape denoting surface slope α and linestyle denoting γ . Middle row (b–d, f–h): Non-dimensionalized stresses in the three regions of upstream boundary layer, patch interior, and downstream boundary layer, each with analytical solution (solid black curve; equation (47)). Profiles with $\delta = [x]/\ell < 0.3$ are shown and collapse well onto the 1d model. Bottom row (c–d, g–h): Log-log plots showing $\max|\bar{\tau}_{xx}| = \kappa \rho g \alpha \ell / 4$ and decay lengthscale $DL = \kappa [x]$, with proportionality constants κ_5 , κ_6 (Newtonian) and κ_7 , κ_8 (Glen). Asymmetric error bounds (gray shade) denote the 16th–84th percentile of prefactor estimates. To comply with the modeling assumptions, we have restricted all plots, including the log-log plots, to display simulation results satisfying $h < [x] < \ell$.

lengthscale of $(2Bh/C)^{n/(n+1)}$.

Though the stress decay lengthscale increases with the local ice thickness, the exponential nature of the stress response suggests that we should be particular in our definition of the term ‘coupling length’. Say, for example, we are interested in the absolute distance over which the perturbed upstream stress is above a critical value τ_{val} , such that hydrofracture-triggered lake drainage can occur. This distance, referred to here as the absolute coupling length (ACL), is then a function not only of the stress decay lengthscale but also the maximum magnitude of the stress perturbation. The maximum stress magnitude, and therefore the ACL, are therefore unique functions of location on the ice sheet given a specific (h, α) :

$$\text{ACL} = \frac{(2Bh/C)^{n/(n+1)}}{n^{-1/(n+1)}} \ln\left(\frac{\rho g \alpha \ell / 4}{\tau_{val}}\right) \quad (48)$$

As an illustrative example, we use $\tau_{val} = 30$ kPa due to the onset of fracture initiation in linear elastic fracture modeling (LEFM) of ice (e.g., Lai and others, 2020). Note that more sophisticated mechanistic understanding of the critical stress required for hydrofracture-triggered lake drainage is needed to determine τ_{val} . ACL would decrease with τ_{val} so if one were to use $\tau_{val} = 100$ kPa the resulting absolute coupling length would be even smaller. Using (48) we generate phase spaces that demonstrate the sensitivity of the ACL to different parameter combinations in our model (Figure 5). In particular, we assume a fixed patch length of $\ell = 5$ km and display ACL as a function of thickness h and slope α (Figure 5a,b) and then assume a fixed surface slope and display ACL as a function of thickness h and patch length ℓ (Figure 5c,d). For all phasespaces, we assume a sliding ratio of $\gamma = 0.1$. In all panels of Figure 5, the dash-dot curve in each panel marks the $\delta = [x]/\ell = 1$ line, as a reference for the location on the phasespace where the boundary layer length exceeds the patch length, and the 1d model deteriorates strongly.

In the top row (Figure 5a,b), the black dashed curves bound the thickness and surface slope consistent with typical GrIS driving stresses in the range $\tau_d = \rho g h \alpha = 50$ to 150 kPa (e.g., Cuffey and Paterson, 2010). Also in the top row, the solid black curve delineates the 90th-percentile (h, α) envelope of the GrIS derived from BedMachine v6 surface and bed topography (Morlighem and others, 2017) and ITS_LIVE (Version 2) surface velocities (Gardner and others, 2025). In particular, we computed the joint distribution of thicknesses h and along-flow surface slope α from BedMachine v6 and ITS_LIVE, respectively. The ice surface field was coarsened and smoothed to a resolution of 1.5 km and surface slopes were computed from this smoothed DEM. The slopes were then projected onto the local ice-flow direction $\hat{u} = (v_x, v_y)/|\mathbf{v}|$ which was obtained from ITS_LIVE, giving the along-flow slope $\alpha = \arctan(|\nabla s \cdot \hat{u}|)$. Locations with

223 speeds $|\mathbf{v}| < 5$ m/yr were excluded. The resulting (h, α) pairs over grounded ice were binned (120×120
 224 bins spanning $h \in [200, 3000]$ m and $\alpha \in [0.05^\circ, 1.0^\circ]$). The 90th-percentile envelope was then defined as
 225 the smallest set of histogram bins whose cumulative count comprises 90% of all grounded ice pixels. The
 226 boundary of this region was smoothed for visual clarity with a Gaussian filter ($\sigma = 3$ bins) before adding
 227 the contour to the phasespace.

228 In the bottom row (Figure 5c,d), the vertical dashed line marks $\ell = 10$ km, an approximate upper
 229 bound on slippery patch lengths (e.g., Stevens and others, 2015, 2024). The magenta outline traces the
 230 region where these observational and model-validity constraints are simultaneously satisfied. Within this
 231 region, ACLs are up to 14 km for $n = 1$ and up to 12 km for $n = 3$. Accounting for the fitting constant for
 232 the $n = 3$ cases of ~ 2.8 (Figure 4h) could imply the ACL for $n = 3$ cases reaches up to ~ 34 km.

233 To illustrate how the ACL dependencies play out, and indeed compete, in a spatial context, we evaluate
 234 the analytical model along an idealized convex ice sheet profile (e.g., Weertman, 1976). We assume a
 235 perfectly plastic ice sheet with a divide-to-terminus distance of $L = 300$ km resting on a flat bed with
 236 yield stress $\tau_y = 50$ kPa. The thickness and surface slope are thus related by $h(x) = \sqrt{2\tau_y x / (\rho g)}$ and
 237 $\alpha(x) = \tau_y / (\rho g h)$, where x is the distance from the terminus (Figure 6). This profile traces a one-dimensional
 238 path through the phasespace (Figure 5), with a steep thin margin and gentle thick interior.

239 Figure 6a,b shows the ice sheet cross section colored by the ACL and maximum stress magnitude,
 240 respectively, assuming a 5 km slippery patch with $\gamma = 0.1$ and $n = 3$. Tracing from the terminus,
 241 the ACL first increases toward the interior until it reaches a maximum value of ~ 3 km around 75 km
 242 from the terminus, at which point the ACL decreases monotonically toward the interior (Figure 6a,c,d).
 243 Despite the fact that the decay lengthscale, $[x]$, increases with thickness h , we see here the competing
 244 effect of the decreasing stress magnitude. Stress magnitude is a strong function of surface slope α which
 245 decreases monotonically from terminus to interior (Figure 6b,c,d). As a result, the ACL reaches a peak
 246 value somewhere between the interior and the terminus, corresponding to conditions typical of the GrIS
 247 ablation zone which is host to many supraglacial lakes.

248 CONCLUSION

249 We have presented an investigation into the viscous stress response of an ice sheet to a spatially finite
 250 region of basal traction loss, i.e., a slippery patch, using a combination of a depth averaged analytical
 251 model and 2d full-Stokes numerical simulations using Elmer/Ice. Our 1d analytical model, derived from

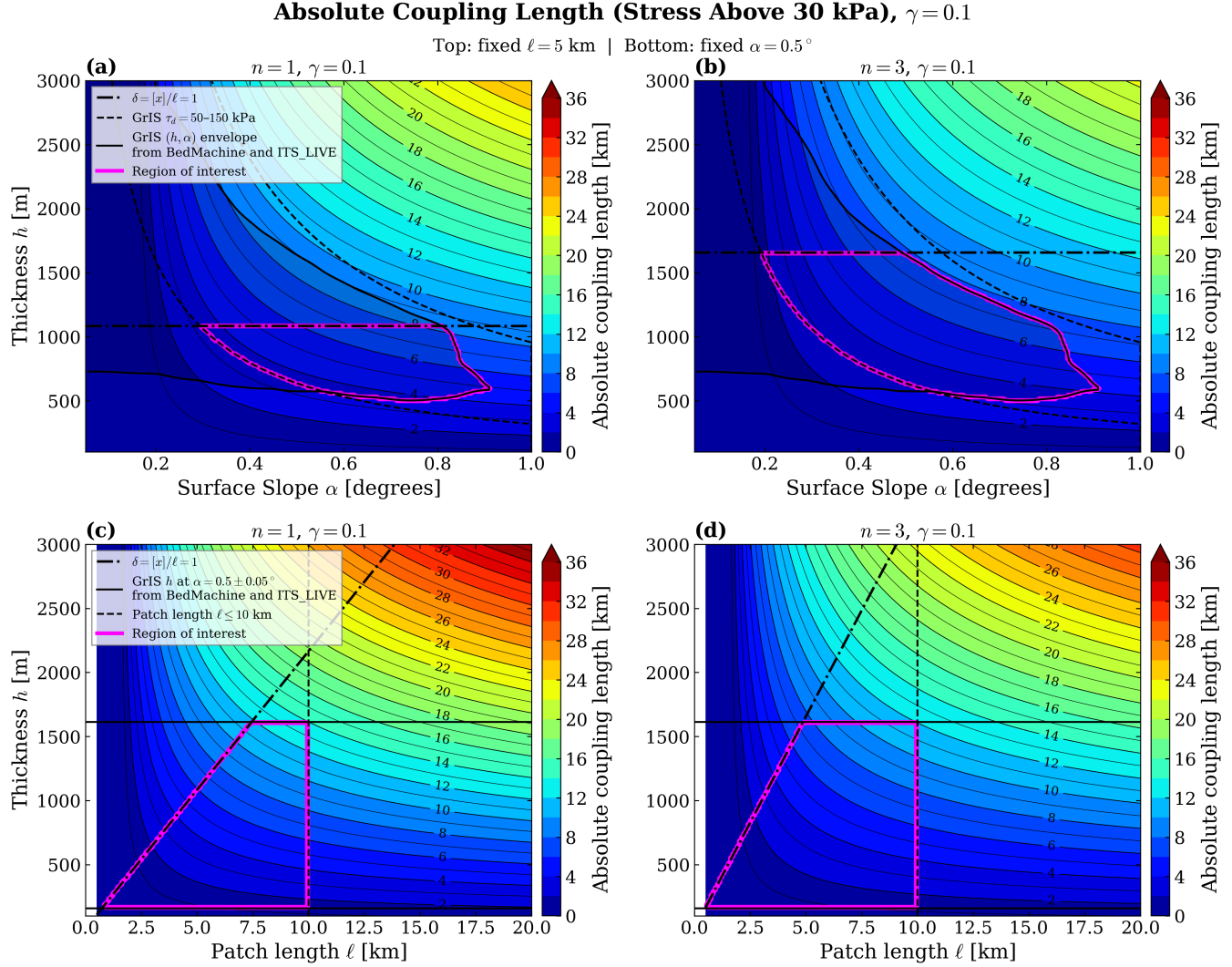


Fig. 5. Phase space maps of the absolute coupling length (ACL, (48)) for the analytical 1d boundary layer model with $\gamma = 0.1$ and stress threshold value $\tau_{val} = 30$ kPa. (a, b) ACL as a function of ice thickness h and surface slope α for a patch length of $\ell = 5$ km for Newtonian ($n = 1$) and Glen ($n = 3$) rheologies, respectively. (c, d) ACL as a function of h and patch length ℓ for a fixed surface slope $\alpha = 0.5^\circ$. In all panels, the black dash-dot curve marks the boundary where $\delta = 1$, outside of which the boundary layer lengthscale exceeds the patch length ($\delta > 1$) and the 1d model breaks down significantly for the Glen rheology (equations 22, 23). In (a, b) the black dashed curves bound typical GrIS driving stress range $\tau_d = \rho g h \alpha$ between 50 and 150 kPa; the solid black contour delineates the 90th percentile envelope of (h, α) values derived from BedMachine v6 (Morlighem and others, 2017) and ITS_LIVE (Gardner and others, 2025). In (c, d), the vertical dashed line marks the $\ell = 10$ km, an approximate upper bound for slippery patches, and the solid horizontal lines bound the 5th-95th percentile thickness range of GrIS grounded ice pixels with along flow slope $\alpha = 0.5^\circ \pm 0.05^\circ$. The magenta outline traces the region where all observational and model validity constraints are simultaneously satisfied, and thus is the region of interest in the phase space.

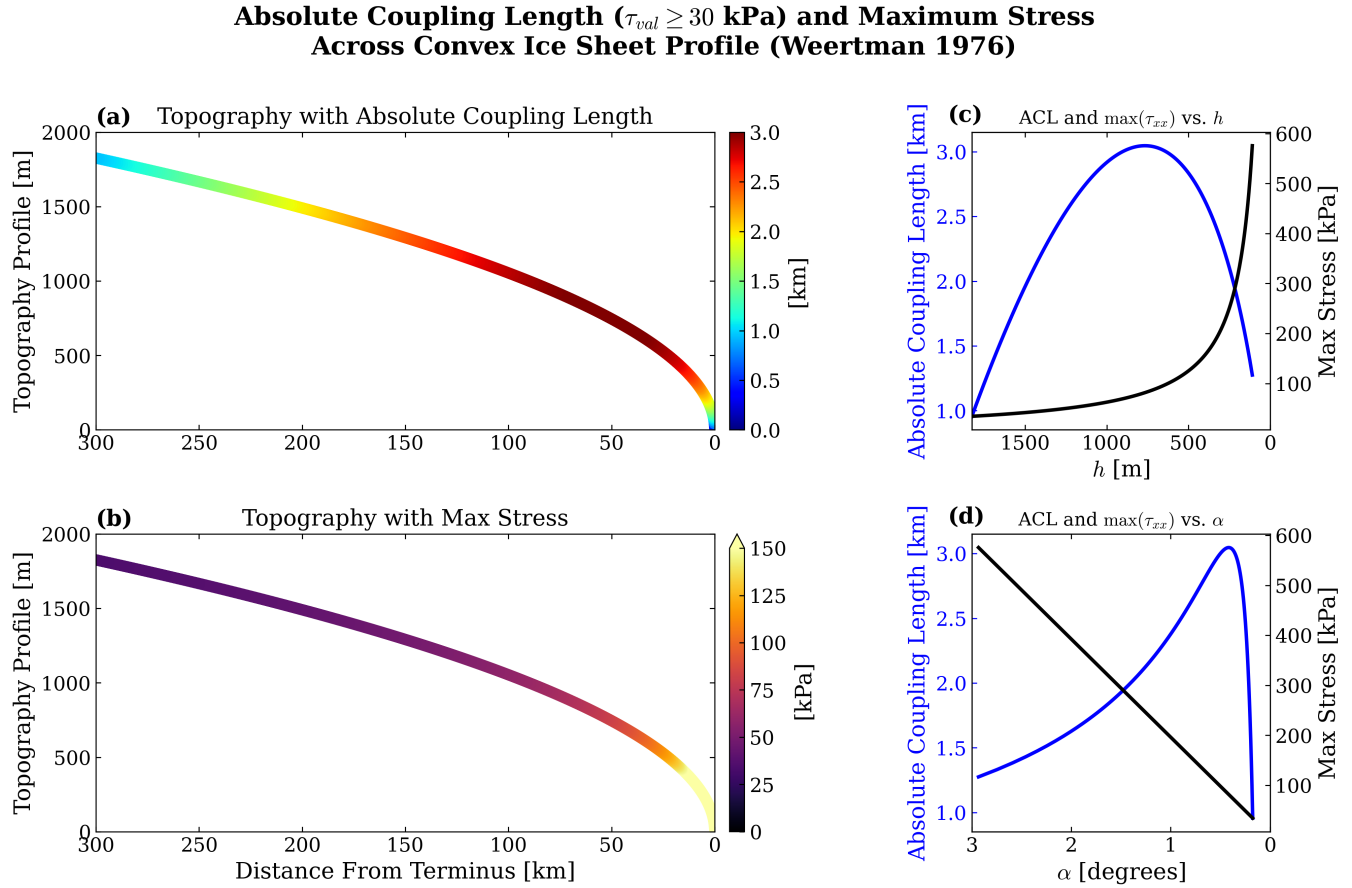


Fig. 6. Absolute coupling length (ACL) and maximum longitudinal deviatoric stress τ_{xx} evaluated along an idealized convex ice sheet profile (Weertman, 1976) with divide-to-terminus distance $L = 300$ km, yield stress $\tau_y = 50$ kPa, Glen ($n = 3$) rheology, sliding ratio $\gamma = 0.1$, patch length $\ell = 5$ km, and stress threshold $\tau_{val} = 30$ kPa (48). (a) Surface topography colored by ACL, showing a peak of ~ 3 km in the ablation zone ~ 75 km from the terminus before declining toward the interior. (b) Same topography colored by the maximum stress magnitude $\max \tau_{xx} = \rho g \alpha \ell / 4$, which decreases monotonically from the margin toward the flattening interior. (c) ACL (blue, left axis) and maximum stress (black, right axis) as functions of ice thickness h , demonstrating competing effects of increasing decay lengthscale and decreasing stress magnitude with growing thickness. (d) ACL and stress maximum as functions of slope.

252 SSA, reveals that the perturbed stress is governed by two fundamental scales: the stress magnitude scales
 253 as $\rho g \alpha \ell / 4$, set by the driving stress and patch length, while the spatial decay of the perturbation extends
 254 over a decay lengthscale $(2Bh/C)^{n/(n+1)}$. The latter scale is set by the balance between membrane stress
 255 gradients and basal drag. These scalings hold for the two rheologies tested, namely Newtonian $n = 1$ and
 256 Glen $n = 3$, for both depth-averaged and surface stresses. Our 1d theory of the stress perturbation profiles
 257 agrees well with depth-averaged simulations. Numerical deviations from the 1d model are stronger for the
 258 Glen rheology, which is expected due to the model's inexactness and dependence on δ (Equations 29, 30).
 259 This dependence is further confirmed in Appendix C (see Figure C1).

260 Together, the stress magnitude and decay length determine an absolute coupling length (ACL), which
 261 we define to be the distance over which the stress perturbation exceeds some defined threshold. Evaluation
 262 of the ACL along an idealized ice sheet profiles reveals a non-monotonic dependence on distance from the
 263 terminus (Figure 6). In particular, despite the decay length growing with ice thickness as derived in the
 264 1d model and confirmed by the numerical studies, the rapidly diminishing surface slope in the ice interior
 265 drives a competing reduction in stress magnitude, such that the ACL reaches a peak in the ablation zone,
 266 the region which is home to many supraglacial lakes. The same qualitative conclusion holds from the
 267 estimated absolute coupling length over the Greenland Ice Sheet in figure A1 in Appendix A.

268 With these results, we aim to contribute to the ongoing discussion of lake drainage communication and
 269 cascade dynamics. Our simple model provides a transparent, parameter-explicit, idealized understanding
 270 of the structure of a stress perturbation from a basal slippery patch and how this structure varies across
 271 an idealized ice sheet. The finding that the ACLs are largest in the ablation zone, perhaps up to a few tens
 272 of kilometers when accounting for the $n = 3$ numerical prefactor, supports the plausibility of membrane
 273 stress transmission across the ice and possible triggering between neighboring lakes.

274 Though the presence of supraglacial lakes is expected to continue expanding inland from the GrIS
 275 margin under the warming climate (e.g., Leeson and others, 2015), these inland locations may indeed be
 276 more shielded from the same hydrofracture cascade effects modeled and observed for lakes closer to the
 277 margin in the current ablation zone (e.g., Christoffersen and others, 2018). Stress perturbations inland
 278 may be of smaller magnitude, with shorter ACLs despite the thicker ice. Inland lakes then may be less
 279 likely to drain via hydrofracture, and the ones that do may be less likely to trigger cascades with nearby
 280 lakes. This is of particular interest given the sensitivity of the inland subglacial system to basal traction
 281 loss (Schoof, 2010; Meierbachtol and others, 2013; Dow and others, 2014; Doyle and others, 2014; Poinar

282 and others, 2015).

283 Several important physical processes are not captured in our present model and represent natural
284 extensions of this work. For one, ours is not a time-dependent model. The transient evolution of the
285 stress perturbation following a lake drainage event, and the timescale over which the perturbation arises
286 and decays, transient effects which would consider the viscoelasticity of ice and the motion of the recently
287 injected subglacial water both vertically and laterally, remain to be characterized. Related, we use a
288 simplified representation of the basal traction, as well as ignoring variation in basal topography, which in
289 our view warrants further analysis. The current work is limited also by being 1d along-flow (2d numerically,
290 but still along-flow) and thus ignores lateral stresses. Addressing these extensions, some of which are the
291 subject of current ongoing and future planned work, will be necessary for a more complete characterization
292 of the impacts of lake drainage-induced injections of meltwater to the GrIS bed.

293 **ACKNOWLEDGMENTS**

294 We thank O. Gagliardini (Grenoble Alpes University) for the helpful advices on Elmer/Ice simulations and
295 N.B. Coffey (Stanford University) for the insightful discussions and support throughout the development
296 of this work. We also thank Laura Stevens (University of Oxford) and Ian Hewitt (University of Oxford)
297 for their support and insight throughout the project. The authors acknowledge partial support from NSF's
298 Office of Polar Programs through OPP-2344690.

299 **APPENDIX A: MODEL APPLICATION**

300 We extend the application of our 1d model from the idealized convex ice sheet profile (figure 6) to the
301 map of the Greenland Ice Sheet. Using BedMachine v6 (Morlighem and others, 2017) and ITS_LIVE
302 (Gardner and others, 2025) to obtain a (h, α) estimates across the ice sheet, as described in the Implications
303 subsection, we project the phasespace values for absolute coupling length (ACL, (figure 5)) and maximum
304 stress magnitude values to the topography of Greenland. Without over-interpretation, it is clear (and not
305 surprising) that the same qualitative patterns as were evident in the idealized convex topography case are
306 again present. Namely, the ACL generally increases initially as we move from the margin towards the
307 ablation zone where many supraglacial lakes are located (Dunmire and others (2021), Dunmire and others
308 (2025); zoom frames figure A1a), before decreasing again toward the ice interior. The stress magnitude is
309 at a maximum near the margin, due to the high surface slopes, and decreases toward the interior (figure

310 A1b). This could imply that the lakes currently residing seasonally in the GrIS ablation zone possess
 311 maximum stress communication potential. If they do continue to form further inland (e.g., Leeson and
 312 others, 2015), their stress communications may become relatively muted.

313 APPENDIX B: VELOCITY

We start this appendix with a brief discussion on velocity details in the Elmer/Ice simulations. We then extend our 1d analytical model to discuss the velocity structure across the domain in response to the slippery patch. In the Elmer/Ice numerical simulations we set the inflow/outflow boundary conditions to be periodic. This results in velocity profiles at the inflow/outflow boundaries are consistent with the sliding-accommodated shallow-ice approximation (SIA) (Figure 2):

$$u(z) = \frac{2B^{-n}}{n+1} (\rho g \alpha)^n \left[h^{n+1} - (h-z)^{n+1} \right] + \left(\frac{\rho g h \alpha}{C_b} \right)^n. \quad (49)$$

To facilitate comparison between the analytical and numerical depth averaged results, we define far-field depth-averaged velocities from the simulations by depth-averaging (49) to yield:

$$u_\infty \equiv \frac{2B^{-n}}{n+2} (\rho g \alpha)^n h^{n+1} + \left(\frac{\rho g h \alpha}{C_b} \right)^n. \quad (50)$$

314 This is the background velocity, u_∞ , which is subtracted from the full velocity to characterize the perturbed
 315 velocity, u' .

Another important note is that in order to map the analytical depth-integrated model to the 2d numerical Elmer simulations, a relationship between the parameterizations for the basal shear stress between the two models must be made. In particular, the analytical model uses $\tau_b = C u^{1/n}$ while the Elmer simulation uses $\tau_b = C_b u_b^{1/n}$, giving rise to the relationship between the two parameterizations:

$$C = C_b \left(\frac{u_b}{u} \right)^{1/n}, \quad (51)$$

where, evaluating equations 50 and 49 at $z = 0$ reveals the ratio

$$\left(\frac{u_b}{u} \right) = \frac{n+2}{n+2+2B^{-n}hC_b^n}. \quad (52)$$

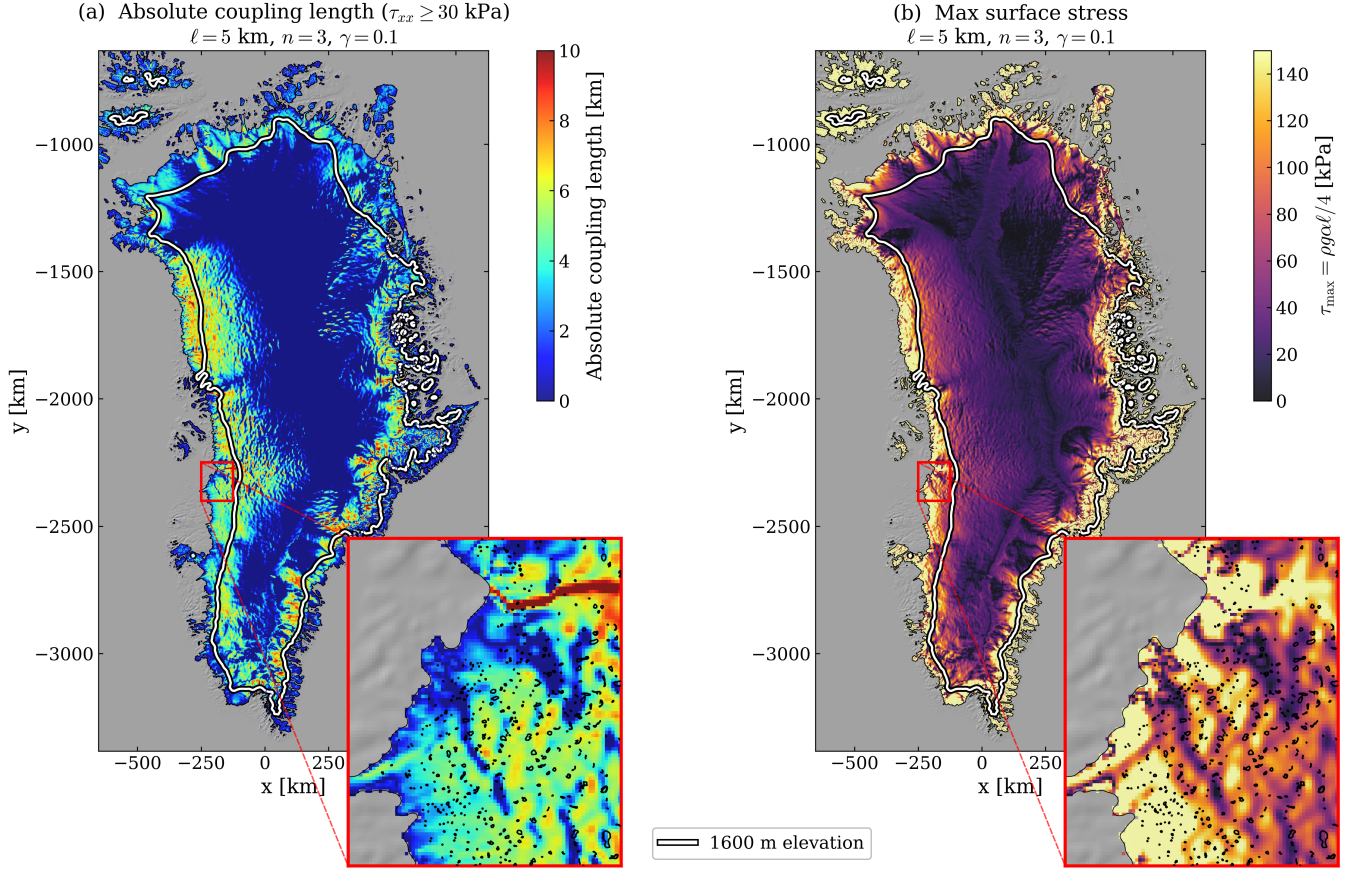


Fig. A1. Application of the 1d boundary layer model to Greenland Ice Sheet conditions using Glen rheology ($n = 3$, $A = 24 \times 10^{-25} \text{ Pa}^{-3} \text{ s}^{-1}$ assuming sliding ratio $\gamma = 0.1$ and fixed patch length $\ell = 5$ km. (a) Absolute coupling length (distance over which $\tau_{xx} \geq \tau_{val} = 30$ kPa; (48)) at each ice pixel, computed from BedMachine v6 ice thickness and ITS_LIVE along flow surface slope, plotted over hillshade basemap. (b) Maximum surface stress $\max \tau_{xx} = \rho g a \ell / 4$ at every ice pixel. Insets show zoomed view of the central west region (red boxes), with black polygons outlining observed supraglacial lakes in the ablation zone (Dunmire and others, 2025). 1600 m elevation contour shown in white, representing the approximate current-day upper bound of lake presence (e.g., Poinar and others, 2015; Fan and others, 2025).

We now present the 1d model for the velocity field. Outside the patch, we have already encountered the velocity solution as an intermediate step in deriving stress (44). For the velocity across the patch, we begin by recalling the dimensional linear deviatoric stress profile across the patch (10):

$$\tau_{xx}(x) = \frac{\rho g \alpha \ell}{4} \left(1 - \frac{2x}{\ell}\right) = \frac{\tau_d \ell}{4h} \left(1 - \frac{2x}{\ell}\right), \quad (53)$$

where again we have returned to dimensional variables. We obtain the velocity gradient from the constitutive relation $\tau_{xx} = B|u_x|^{1/n-1}u_x$ (recalling that $u_x = u'_x$ because u_∞ is constant):

$$u'_x = \left| \frac{\tau_{xx}}{B} \right|^{n-1} \frac{\tau_{xx}}{B}. \quad (54)$$

We substitute the linear stress profile (53) which gives:

$$u'_x = \left(\frac{\tau_d \ell}{4Bh} \right)^n \left| 1 - \frac{2x}{\ell} \right|^{n-1} \left(1 - \frac{2x}{\ell} \right). \quad (55)$$

We introduce dimensionless variables:

$$\tilde{u}' = \frac{u'}{[u]}, \quad \xi = \frac{x}{\ell}, \quad (56)$$

where $[u] = [x](\tau_d \ell / (4Bh))^n$ (18). Converting the x derivative using $u'_x = (1/\ell)du'/d\xi$ and substituting the dimensionless variables (56):

$$\frac{[u]}{\ell} \frac{d\tilde{u}'}{d\xi} = \left(\frac{\tau_d \ell}{4Bh} \right)^n |1 - 2\xi|^{n-1} (1 - 2\xi). \quad (57)$$

Dropping tildes, and recalling that $[u] = [x](\tau_d \ell / (4Bh))^n$ (18) allows us to write:

$$\frac{[x]}{\ell} \left(\frac{\tau_d \ell}{4Bh} \right)^n \frac{du'}{d\xi} = \left(\frac{\tau_d \ell}{4Bh} \right)^n |1 - 2\xi|^{n-1} (1 - 2\xi). \quad (58)$$

The $(\tau_d \ell / (4Bh))^n$ factors cancel, leaving

$$\frac{du'}{d\xi} = \frac{\ell}{[x]} |1 - 2\xi|^{n-1} (1 - 2\xi) = \frac{1}{\delta} |1 - 2\xi|^{n-1} (1 - 2\xi), \quad (59)$$

where $\delta = [x]/\ell$ (23). We integrate from $\xi = 0$, where $u'(0) = u'_0 = (1/n)^{n/(n+1)}$ is the velocity at the patch

edge (43):

$$u'(\xi) = u'_0 + \frac{1}{\delta} \int_0^\xi |1 - 2\xi'|^{n-1} (1 - 2\xi') d\xi'. \quad (60)$$

We note that the antiderivative of $|1 - 2\xi|^{n-1}(1 - 2\xi)$ with respect to ξ is $-\frac{|1-2\xi|^{n+1}}{2(n+1)}$, which can be verified by considering two cases separately. For $\xi < 1/2$, $|1 - 2\xi| = (1 - 2\xi)$, so:

$$\frac{d}{d\xi} \left(-\frac{(1 - 2\xi)^{n+1}}{2(n+1)} \right) = -\frac{(n+1)(1 - 2\xi)^n \cdot (-2)}{2(n+1)} = (1 - 2\xi)^n = |1 - 2\xi|^{n-1}(1 - 2\xi). \quad (61)$$

For $\xi > 1/2$, $|1 - 2\xi| = (2\xi - 1)$, so:

$$\frac{d}{d\xi} \left(-\frac{(2\xi - 1)^{n+1}}{2(n+1)} \right) = -\frac{(n+1)(2\xi - 1)^n \cdot 2}{2(n+1)} = -(2\xi - 1)^n = |1 - 2\xi|^{n-1}(1 - 2\xi), \quad (62)$$

where in the last step we used $(1 - 2\xi) < 0$ for $\xi > 1/2$, so $|1 - 2\xi|^{n-1}(1 - 2\xi) = (2\xi - 1)^{n-1} \cdot (-(2\xi - 1)) = -(2\xi - 1)^n$. With this, we integrate directly:

$$u'(\xi) = u'_0 + \frac{1}{\delta} \int_0^\xi |1 - 2\xi'|^{n-1} (1 - 2\xi') d\xi' \quad (63)$$

$$= u'_0 + \frac{1}{\delta} \left[-\frac{|1 - 2\xi'|^{n+1}}{2(n+1)} \right]_0^\xi \quad (64)$$

$$= u'_0 + \frac{1}{\delta} \left(-\frac{|1 - 2\xi|^{n+1}}{2(n+1)} + \frac{1}{2(n+1)} \right) \quad (65)$$

$$= u'_0 + \frac{1}{2(n+1)\delta} [1 - |1 - 2\xi|^{n+1}] \quad (66)$$

where $u'_0 = (1/n)^{n/(n+1)}$ is the velocity at the patch edge (43). The velocity is symmetric about the patch center $\xi = 1/2$, where it reaches its maximum value:

$$u'_{max} = u'_0 + \frac{1}{2(n+1)\delta} = (1/n)^{n/(n+1)} + \frac{1}{2(n+1)\delta} \quad (67)$$

Below we derive a suitable normalization for the velocity perturbation within the patch. Subtracting the velocity maximum (67) from the patch-interior equation (66):

$$u'(\xi) - u'_{max} = -\frac{1}{2(n+1)\delta} |1 - 2\xi|^{n+1}. \quad (68)$$

Returning to dimensional variables using $u' = [u]\tilde{u}'$, $\xi = x/\ell$, and $[u] = [x](\tau_d \ell / (4Bh))^n$ (18), and noting

that $1/\delta = \ell/[x]$, the factors of $[x]$ cancel to give

$$\frac{u' - u'_{\max}}{(\rho g \alpha \ell / 4B)^n \ell} = -\frac{2^n}{n+1} \left| \frac{x}{\ell} - \frac{1}{2} \right|^{n+1}. \quad (69)$$

316 The right-hand side depends only on x/ℓ : the velocity shape within the patch is independent of the basal
317 sliding coefficient C and the coupling length $[x]$, which enter only through the peak amplitude u'_{\max} .

Thus, for comparison between the numerical and analytical curves across the patch, the depth-averaged numerical velocity magnitudes are shifted by the maximum velocity u'_{\max} and normalized by $(\rho g \alpha \ell / 4B)^n \ell$, such that all curves collapse regardless of δ onto the analytical curve (black curves, figure B1b,f,c,g). The perturbed velocity in the upstream and downstream boundary layer regions, derived in the main text (44), is rescaled by the perturbed velocity at the patch edge u'_0 , such that the dimensionless velocity at the patch edges is unity. The velocity decay length outside the patch, like the stresses, is characterized by $[x]$ (16). In summary, the velocity model across the domain is expressed as:

$$\boxed{\begin{aligned} \frac{u'(x)}{u'_0} &= \exp\left(n \frac{x}{[x]}\right), & x \leq 0 \\ \frac{u' - u'_{\max}}{(\rho g \alpha \ell / 4B)^n \ell} &= -\frac{2^n}{n+1} \left| \frac{x}{\ell} - \frac{1}{2} \right|^{n+1}, & 0 \leq x \leq \ell \\ \frac{u'(x)}{u'_0} &= \exp\left(-n \frac{(x-\ell)}{[x]}\right), & x \geq \ell, \end{aligned}} \quad (70)$$

318 where the theoretical patch-edge velocity $u'_0 = [u](1/n)^{n/(n+1)}$ and the theoretical maximum perturbed
319 velocity u'_{\max} are defined in equations (43) and (67) respectively.

320 APPENDIX C: MODEL SENSITIVITY

321 The 1d model is asymptotically valid only where $\delta = [x]/\ell \ll 1$. This requirement bears little significance to
322 the case of Newtonian rheology (equations 29, 30), but becomes important for $n > 1$ (e.g., Glen rheology).
323 Thus, the 1d model offers an approximation of the depth-averaged flow which is of increasing fidelity as δ
324 diminishes. This dependence on δ can be clearly explained and visualized by coloring the nondimensional
325 curves (as in figures 4 and B1) by their corresponding δ value, as we do here in figure C1.

Depth-Averaged Perturbation Velocity

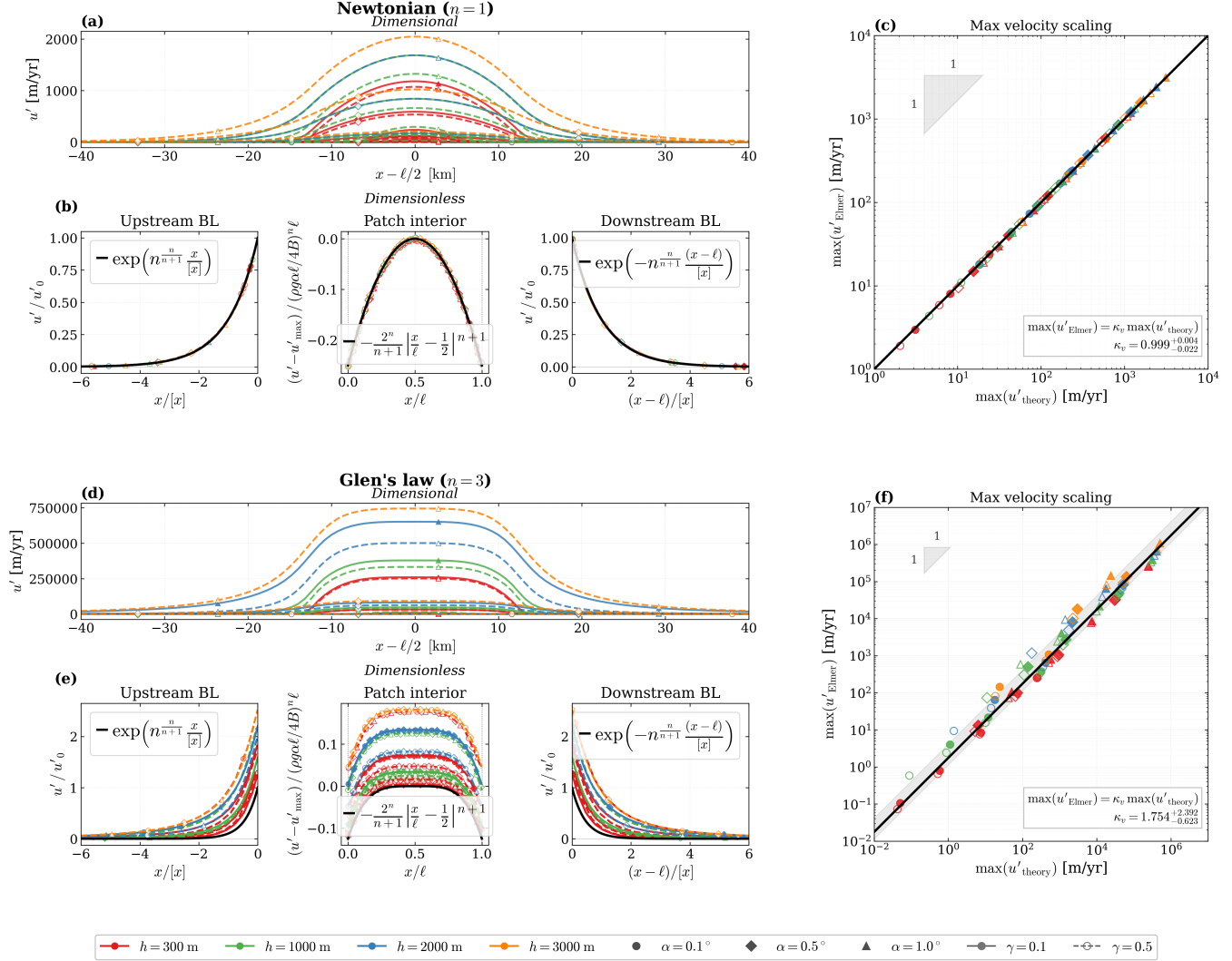


Fig. B1. Depth-averaged velocity profiles from the 2d Elmer/Ice simulation ensemble (colored curves) and comparison to 1d analytical model ((70), black curves) for experiments with Newtonian and Glen rheologies on the top and bottom, respectively, with (a, d) showing dimensional velocities from the simulations; (b, e) showing non-dimensionalized results; (c, f) showing log-scale plots comparing theoretical maximum velocity (67) to maximum simulated velocity. All velocities are perturbed velocities (u') above background (u_∞), where the background velocities are defined by the theory (50). Note that the same (as for stress, figures 3, 4) threshold of $\delta < 0.3$ was applied for the profiles in (a, e) and the threshold of $h < [x] < \ell$ applied for all plots, including the log-log plots in (d, h).

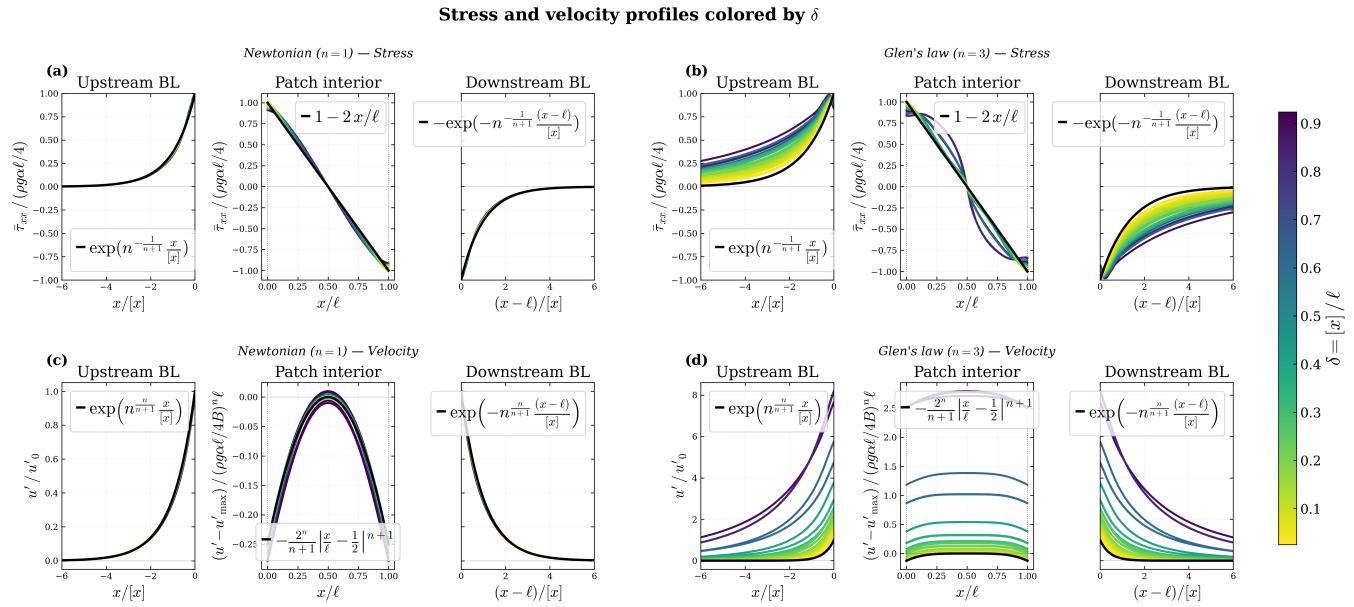


Fig. C1. Non-dimensional depth-averaged profiles for stress (top row) and velocity (bottom row) for the Newtonian and Glen rheology experiments (left, right, respectively) for which $h, \delta \leq 1$. Experiments with smaller δ values exhibit tighter agreement with the 1d analytical theory (black), as expected. Only the $h < [x] < \ell$ filter was applied to the curves here.

326 REFERENCES

- 327 Alley RB, Dupont TK, Parizek BR and Anandakrishnan S (2005) Access of surface meltwater to beds of
 328 sub-freezing glaciers: preliminary insights. *Annals of Glaciology*, **40**, 8–14, ISSN 0260-3055, 1727-5644 (doi:
 329 10.3189/172756405781813483)
- 330 Barcilon V and MacAyeal DR (1993) Steady flow of a viscous ice stream across a no-slip/free-slip transition at the
 331 bed. *Journal of Glaciology*, **39**(131), 167–185, ISSN 0022-1430, 1727-5652 (doi: 10.3189/S0022143000015811)
- 332 Bindschadler R and Vornberger P (1998) Changes in the West Antarctic Ice Sheet Since 1963 from Declassified
 333 Satellite Photography. *Science*, **279**(5351), 689–692 (doi: 10.1126/science.279.5351.689)
- 334 Chandler DM, Wadham JL, Lis GP, Cowton T, Sole A, Bartholomew I, Telling J, Nienow P, Bagshaw EB, Mair
 335 D, Vinen S and Hubbard A (2013) Evolution of the subglacial drainage system beneath the Greenland Ice Sheet
 336 revealed by tracers. *Nature Geoscience*, **6**(3), 195–198, ISSN 1752-0894, 1752-0908 (doi: 10.1038/ngeo1737)
- 337 Christoffersen P, Bougamont M, Hubbard A, Doyle SH, Grigsby S and Petterson R (2018) Cascading lake drainage
 338 on the Greenland Ice Sheet triggered by tensile shock and fracture. *Nature Communications*, **9**(1), 1064, ISSN
 339 2041-1723 (doi: 10.1038/s41467-018-03420-8)

- 340 Chugunov VA and Wilchinsky AV (1996) Modelling of a marine glacier and ice-sheet-ice-shelf transition
341 zone based on asymptotic analysis. *Annals of Glaciology*, **23**, 59–67, ISSN 0260-3055, 1727-5644 (doi:
342 10.3189/S0260305500013264)
- 343 Crozier J, Karlstrom L and Yang K (2018) Basal control of supraglacial meltwater catchments on the Greenland Ice
344 Sheet. *The Cryosphere*, **12**(10), 3383–3407, ISSN 1994-0416 (doi: 10.5194/tc-12-3383-2018)
- 345 Cuffey KM and Paterson WSB (2010) *The Physics of Glaciers*. Butterworth-Heinemann, Oxford, 4 edition
- 346 Das SB, Joughin I, Behn MD, Howat IM, King MA, Lizarralde D and Bhatia MP (2008) Fracture Propagation
347 to the Base of the Greenland Ice Sheet During Supraglacial Lake Drainage. *Science*, **320**(5877), 778–781 (doi:
348 10.1126/science.1153360)
- 349 Dow CF, Kulesa B, Rutt IC, Doyle SH and Hubbard A (2014) Upper bounds on subglacial channel development for
350 interior regions of the Greenland ice sheet. *Journal of Glaciology*, **60**(224), 1044–1052, ISSN 0022-1430, 1727-5652
351 (doi: 10.3189/2014JoG14J093)
- 352 Doyle SH, Hubbard A, Fitzpatrick AAW, van As D, Mikkelsen AB, Pettersson R and Hubbard
353 B (2014) Persistent flow acceleration within the interior of the Greenland ice sheet. *Geophys-
354 ical Research Letters*, **41**(3), 899–905, ISSN 1944-8007 (doi: 10.1002/2013GL058933), _eprint:
355 <https://onlinelibrary.wiley.com/doi/pdf/10.1002/2013GL058933>
- 356 Dunmire D, Banwell AF, Wever N, Lenaerts JTM and Datta RT (2021) Contrasting regional variability of buried
357 meltwater extent over 2 years across the Greenland Ice Sheet. *The Cryosphere*, **15**(6), 2983–3005, ISSN 1994-0424
358 (doi: 10.5194/tc-15-2983-2021)
- 359 Dunmire D, Subramanian AC, Hossain E, Gani MO, Banwell AF, Younas H and Myers B (2025) Greenland
360 Ice Sheet Wide Supraglacial Lake Evolution and Dynamics: Insights From the 2018 and 2019 Melt Sea-
361 sons. *Earth and Space Science*, **12**(2), e2024EA003793, ISSN 2333-5084 (doi: 10.1029/2024EA003793), _eprint:
362 <https://onlinelibrary.wiley.com/doi/pdf/10.1029/2024EA003793>
- 363 Fan Y, Ke CQ, Luo L, Shen X, Livingstone SJ and Lea JM (2025) Expansion of supraglacial lake area, volume and
364 extent on the Greenland ice sheet from 1985 to 2023. *Journal of Glaciology*, **71**, e4, ISSN 0022-1430, 1727-5652
365 (doi: 10.1017/jog.2024.87)
- 366 Fitzpatrick AaW, Hubbard AL, Box JE, Quincey DJ, van As D, Mikkelsen APB, Doyle SH, Dow CF, Hasholt B and
367 Jones GA (2014) A decade (2002–2012) of supraglacial lake volume estimates across Russell Glacier, West
368 Greenland. *The Cryosphere*, **8**(1), 107–121, ISSN 1994-0416 (doi: 10.5194/tc-8-107-2014)

- 369 Gagliardini O, Zwinger T, Gillet-Chaulet F, Durand G, Favier L, de Fleurian B, Greve R, Malinen M, Martín C,
370 Råback P, Ruokolainen J, Sacchettini M, Schäfer M, Seddik H and Thies J (2013) Capabilities and performance of
371 Elmer/Ice, a new-generation ice sheet model. *Geoscientific Model Development*, **6**(4), 1299–1318, ISSN 1991-959X
372 (doi: 10.5194/gmd-6-1299-2013)
- 373 Gardner AS, Greene CA, Kennedy JH, Fahnestock MA, Liukis M, López LA, Lei Y, Scambos TA and Dehecq A
374 (2025) ITS_live global glacier velocity data in near-real time. *The Cryosphere*, **19**(9), 3517–3533, ISSN 1994-0416
375 (doi: 10.5194/tc-19-3517-2025)
- 376 Glen JW (1955) The creep of polycrystalline ice. *Proceedings of the Royal Society of London. Series A. Mathematical
377 and Physical Sciences*, **228**(1175), 519–538 (doi: 10.1098/rspa.1955.0066)
- 378 Gudmundsson GH (2003) Transmission of basal variability to a glacier surface. *Journal of Geophysical Research:
379 Solid Earth*, **108**(B5), ISSN 2156-2202 (doi: 10.1029/2002JB002107)
- 380 Gudmundsson GH (2008) Analytical solutions for the surface response to small amplitude perturbations in boundary
381 data in the shallow-ice-stream approximation. *The Cryosphere*, **2**(2), 77–93, ISSN 1994-0416 (doi: 10.5194/tc-2-
382 77-2008)
- 383 Haseloff M, Schoof C and Gagliardini O (2015) A boundary layer model for ice stream margins. *Journal of Fluid
384 Mechanics*, **781**, 353–387, ISSN 0022-1120, 1469-7645 (doi: 10.1017/jfm.2015.503)
- 385 Hulbe C and Fahnestock M (2007) Century-scale discharge stagnation and reactivation of the Ross ice
386 streams, West Antarctica. *Journal of Geophysical Research: Earth Surface*, **112**(F3), ISSN 2156-2202 (doi:
387 10.1029/2006JF000603), _eprint: <https://onlinelibrary.wiley.com/doi/pdf/10.1029/2006JF000603>
- 388 Ignéczi Sole AJ, Livingstone SJ, Leeson AA, Fettweis X, Selmes N, Gourmelen N and Briggs K (2016) Northeast
389 sector of the Greenland Ice Sheet to undergo the greatest inland expansion of supraglacial lakes during the 21st
390 century. *Geophysical Research Letters*, **43**(18), 9729–9738, ISSN 1944-8007 (doi: 10.1002/2016GL070338), _eprint:
391 <https://onlinelibrary.wiley.com/doi/pdf/10.1002/2016GL070338>
- 392 Jacobson HP and Raymond CF (1998) Thermal effects on the location of ice stream margins. *Journal of Geo-
393 physical Research: Solid Earth*, **103**(B6), 12111–12122, ISSN 2156-2202 (doi: 10.1029/98JB00574), _eprint:
394 <https://onlinelibrary.wiley.com/doi/pdf/10.1029/98JB00574>
- 395 Joughin I, Das SB, Flowers GE, Behn MD, Alley RB, King MA, Smith BE, Bamber JL, van den Broeke MR and
396 van Angelen JH (2013) Influence of ice-sheet geometry and supraglacial lakes on seasonal ice-flow variability. *The
397 Cryosphere*, **7**(4), 1185–1192, ISSN 1994-0424 (doi: 10.5194/tc-7-1185-2013)

- 398 Kamb B and Echelmeyer KA (1986) Stress-Gradient Coupling in Glacier Flow: I. Longitudinal Averaging of the
399 Influence of Ice Thickness and Surface Slope. *Journal of Glaciology*, **32**(111), 267–284, ISSN 0022-1430, 1727-5652
400 (doi: 10.3189/S0022143000015604)
- 401 Lai CY, Kingslake J, Wearing MG, Chen PHC, Gentine P, Li H, Spergel JJ and van Wessem JM (2020) Vulnera-
402 bility of Antarctica’s ice shelves to meltwater-driven fracture. *Nature*, **584**(7822), 574–578, ISSN 1476-4687 (doi:
403 10.1038/s41586-020-2627-8)
- 404 Lai CY, Stevens LA, Chase DL, Creyts TT, Behn MD, Das SB and Stone HA (2021) Hydraulic transmissivity
405 inferred from ice-sheet relaxation following Greenland supraglacial lake drainages. *Nature Communications*, **12**(1),
406 3955, ISSN 2041-1723 (doi: 10.1038/s41467-021-24186-6), number: 1
- 407 Leeson AA, Shepherd A, Briggs K, Howat I, Fettweis X, Morlighem M and Rignot E (2015) Supraglacial lakes on the
408 Greenland ice sheet advance inland under warming climate. *Nature Climate Change*, **5**(1), 51–55, ISSN 1758-6798
409 (doi: 10.1038/nclimate2463), number: 1
- 410 MacAyeal DR (1989) Large-scale ice flow over a viscous basal sediment: Theory and application to ice stream
411 B, Antarctica. *Journal of Geophysical Research: Solid Earth*, **94**(B4), 4071–4087, ISSN 01480227 (doi:
412 10.1029/JB094iB04p04071)
- 413 MacFerrin M, Machguth H, As Dv, Charalampidis C, Stevens CM, Heilig A, Vandecrux B, Langen PL, Mottram R,
414 Fettweis X, Broeke MRvd, Pfeffer WT, Moussavi MS and Abdalati W (2019) Rapid expansion of Greenland’s low-
415 permeability ice slabs. *Nature*, **573**(7774), 403–407, ISSN 1476-4687 (doi: 10.1038/s41586-019-1550-3), number:
416 7774
- 417 Mantelli E, Haseloff M and Schoof C (2019) Ice sheet flow with thermally activated sliding. Part 1: the role of
418 advection. *Proceedings. Mathematical, Physical, and Engineering Sciences*, **475**(2230), 20190410, ISSN 1364-5021
419 (doi: 10.1098/rspa.2019.0410)
- 420 Meierbachtol T, Harper J and Humphrey N (2013) Basal Drainage System Response to Increasing Surface Melt on
421 the Greenland Ice Sheet. *Science*, **341**(6147), 777–779 (doi: 10.1126/science.1235905)
- 422 Morlighem M, Williams CN, Rignot E, An L, Arndt JE, Bamber JL, Catania G, Chauché N, Dowdeswell JA,
423 Dorschel B, Fenty I, Hogan K, Howat I, Hubbard A, Jakobsson M, Jordan TM, Kjeldsen KK, Millan R, Mayer L,
424 Mougintot J, Noël BPY, O’Cofaigh C, Palmer S, Rysgaard S, Seroussi H, Siegert MJ, Slabon P, Straneo F, van den
425 Broeke MR, Weinrebe W, Wood M and Zinglensen KB (2017) BedMachine v3: Complete Bed Topography and
426 Ocean Bathymetry Mapping of Greenland From Multibeam Echo Sounding Combined With Mass Conservation.
427 *Geophysical Research Letters*, **44**(21), 11,051–11,061, ISSN 1944-8007 (doi: 10.1002/2017GL074954), _eprint:
428 <https://agupubs.onlinelibrary.wiley.com/doi/pdf/10.1002/2017GL074954>

- 429 Poinar K and Andrews LC (2021) Challenges in predicting Greenland supraglacial lake drainages at the regional
430 scale. *The Cryosphere*, **15**(3), 1455–1483, ISSN 1994-0416 (doi: 10.5194/tc-15-1455-2021)
- 431 Poinar K, Joughin I, Das SB, Behn MD, Lenaerts JTM and van den Broeke MR (2015) Limits
432 to future expansion of surface-melt-enhanced ice flow into the interior of western Greenland. *Geo-
433 physical Research Letters*, **42**(6), 1800–1807, ISSN 1944-8007 (doi: 10.1002/2015GL063192), __eprint:
434 <https://onlinelibrary.wiley.com/doi/pdf/10.1002/2015GL063192>
- 435 Raymond MJ and Gudmundsson GH (2005) On the relationship between surface and basal properties on glaciers,
436 ice sheets, and ice streams. *Journal of Geophysical Research: Solid Earth*, **110**(B8), ISSN 2156-2202 (doi:
437 10.1029/2005JB003681), __eprint: <https://agupubs.onlinelibrary.wiley.com/doi/pdf/10.1029/2005JB003681>
- 438 Rignot E, Mouginot J and Scheuchl B (2011) Ice Flow of the Antarctic Ice Sheet. *Science*, **333**(6048), 1427–1430
439 (doi: 10.1126/science.1208336)
- 440 Schoof C (2007a) Ice sheet grounding line dynamics: Steady states, stability, and hysteresis. *Journal of
441 Geophysical Research: Earth Surface*, **112**(F3), ISSN 2156-2202 (doi: 10.1029/2006JF000664), __eprint:
442 <https://onlinelibrary.wiley.com/doi/pdf/10.1029/2006JF000664>
- 443 Schoof C (2007b) Marine ice-sheet dynamics. Part 1. The case of rapid sliding. *Journal of Fluid Mechanics*, **573**,
444 27–55, ISSN 0022-1120, 1469-7645 (doi: 10.1017/S0022112006003570)
- 445 Schoof C (2010) Ice-sheet acceleration driven by melt supply variability. *Nature*, **468**(7325), 803–806, ISSN 1476-4687
446 (doi: 10.1038/nature09618), number: 7325
- 447 Schoof C and Mantelli E (2021) The role of sliding in ice stream formation. *Proceedings of the Royal Society A:
448 Mathematical, Physical and Engineering Sciences*, **477**(2248), 20200870 (doi: 10.1098/rspa.2020.0870)
- 449 Sergienko OV (2013) Glaciological twins: basally controlled subglacial and supraglacial lakes. *Journal of Glaciology*,
450 **59**(213), 3–8, ISSN 0022-1430, 1727-5652 (doi: 10.3189/2013JoG12J040)
- 451 Sergienko OV (2022) No general stability conditions for marine ice-sheet grounding lines in the presence of feedbacks.
452 *Nature Communications*, **13**(1), 2265, ISSN 2041-1723 (doi: 10.1038/s41467-022-29892-3)
- 453 Stevens LA, Behn MD, McGuire JJ, Das SB, Joughin I, Herring T, Shean DE and King MA (2015) Greenland
454 supraglacial lake drainages triggered by hydrologically induced basal slip. *Nature*, **522**(7554), 73–76, ISSN 1476-
455 4687 (doi: 10.1038/nature14480), number: 7554
- 456 Stevens LA, Behn MD, Das SB, Joughin I, Noël BPY, van den Broeke MR and Herring T (2016) Greenland Ice
457 Sheet flow response to runoff variability. *Geophysical Research Letters*, **43**(21), 11295–11303, ISSN 1944-8007 (doi:
458 10.1002/2016GL070414), __eprint: <https://onlinelibrary.wiley.com/doi/pdf/10.1002/2016GL070414>

- 459 Stevens LA, Das SB, Behn MD, McGuire JJ, Lai CY, Joughin I, Larochelle S and Nettles M (2024) Elastic Stress Cou-
460 pling Between Supraglacial Lakes. *Journal of Geophysical Research: Earth Surface*, **129**(5), e2023JF007481, ISSN
461 2169-9011 (doi: 10.1029/2023JF007481), _eprint: <https://onlinelibrary.wiley.com/doi/pdf/10.1029/2023JF007481>
- 462 Suckale J, Platt JD, Perol T and Rice JR (2014) Deformation-induced melting in the margins of the West Antarc-
463 tic ice streams. *Journal of Geophysical Research: Earth Surface*, **119**(5), 1004–1025, ISSN 2169-9011 (doi:
464 10.1002/2013JF003008), _eprint: <https://agupubs.onlinelibrary.wiley.com/doi/pdf/10.1002/2013JF003008>
- 465 Tsai VC and Rice JR (2010) A model for turbulent hydraulic fracture and application to crack propagation at glacier
466 beds. *Journal of Geophysical Research: Earth Surface*, **115**(F3), ISSN 2156-2202 (doi: 10.1029/2009JF001474),
467 _eprint: <https://agupubs.onlinelibrary.wiley.com/doi/pdf/10.1029/2009JF001474>
- 468 Tsai VC, Stewart AL and Thompson AF (2015) Marine ice-sheet profiles and stability under Coulomb basal condi-
469 tions. *Journal of Glaciology*, **61**(226), 205–215, ISSN 0022-1430, 1727-5652 (doi: 10.3189/2015JoG14J221)
- 470 Weertman J (1957) Deformation of Floating Ice Shelves. *Journal of Glaciology*, **3**(21), 38–42, ISSN 0022-1430, 1727-
471 5652 (doi: 10.3189/S0022143000024710)
- 472 Weertman J (1974) Stability of the Junction of an Ice Sheet and an Ice Shelf. *Journal of Glaciology*, **13**(67), 3–11,
473 ISSN 0022-1430, 1727-5652 (doi: 10.3189/S0022143000023327)
- 474 Weertman J (1976) Milankovitch solar radiation variations and ice age ice sheet sizes. *Nature*, **261**(5555), 17–20,
475 ISSN 1476-4687 (doi: 10.1038/261017a0)